Earth and Planetary Science Letters 578 (2022) 117330

Contents lists available at ScienceDirect

Earth and Planetary Science Letters

www.elsevier.com/locate/epsl

Geophysical and cosmochemical evidence for a volatile-rich Mars

A. Khan [a,b,*], P.A. Sossi [c], C. Liebske [c], A. Rivoldini [d], D. Giardini [a]

[a] Institute of Geophysics, ETH Zürich, Zürich, Switzerland
[b] Physik Institut, University of Zürich, Zürich, Switzerland
[c] Institute of Geochemistry and Petrology, ETH Zürich, Zürich, Switzerland
[d] Royal Observatory of Belgium, Brussels, Belgium

ARTICLE INFO

Article history:
Received 8 August 2021
Received in revised form 29 October 2021
Accepted 1 December 2021
Available online 16 December 2021
Editor: W.B. McKinnon

Keywords:
Mars
InSight
seismology
interior structure
mantle and core composition
core formation

ABSTRACT

Constraints on the composition of Mars principally derive from chemical analyses of a set of Martian meteorites that rely either on determinations of their refractory element abundances or isotopic compositions. Both approaches, however, lead to models of Mars that are unable to self-consistently explain major element chemistry and match its observed geophysical properties, unless *ad hoc* adjustments to key parameters, namely, bulk Fe/Si ratio, core composition, and/or core size are made. Here, we combine geophysical observations, including high-quality seismic data acquired with the InSight mission, with a cosmochemical model to constrain the composition of Mars. We find that the FeO content of Mars' mantle is 13.7±0.4 wt%, corresponding to a Mg# of 0.81±0.01. Because of the lower FeO content of the mantle, compared with previous estimates, we obtain a higher mean core density of 6150±46 kg/m^3 than predicted by recent seismic observations, yet our estimate for the core radius remains consistent around 1840±10 km, corresponding to a core mass fraction of 0.250±0.005. Relying on cosmochemical constraints, volatile element behaviour, and planetary building blocks that match geophysical and isotopic signatures of Martian meteorites, we find that the liquid core is made up of 88.4±3.9 wt% Fe-Ni-Co with light elements making up the rest. To match the mean core density constraint, we predict, based on experimentally-determined thermodynamic solution models, a light element abundance in the range of ≈9 wt% S, ⩾3 wt% C, ⩽2.5 wt% O, and ⩽0.5 wt% H, supporting the notion of a volatile-rich Mars. To accumulate sufficient amounts of these volatile elements, Mars must have formed before the nebular gas dispersed and/or, relative to Earth, accreted a higher proportion of planetesimals from the outer protoplanetary disk where volatiles condensed more readily.

1. Introduction

Of all geophysical methods used to study a planet's structure, seismology is uniquely suited to determine many parameters that are critically important to understand its dynamic behaviour, as dictated by its physical state (density, temperature) and chemical composition. For these reasons, seismology has played a prominent role in the study of Earth's interior. Extraterrestrial seismology saw its advent with the Apollo program and the installation of seismometers on the lunar surface (Lognonné and Johnson, 2007; Khan et al., 2013; Garcia et al., 2019). With the successful landing of InSight (Interior Exploration using Seismic Investigations, Geodesy and Heat Transport) and deployment of SEIS (Seismic Experiment for Interior Structure) on Mars (Lognonné et al., 2019), followed by detection of marsquakes and acquisition of high-quality seismic data since early 2019 (Banerdt et al., 2020; Lognonné et al., 2020; Giardini et al., 2020), Mars represents the second exterrestrial body for which we have seismic data, affording us a unique opportunity to peer inside the planet (Cottaar and Koelemeijer, 2021). A primary goal of the InSight mission is to image the planet's interior structure – the Rosetta stone for deciphering planetary composition, origin, and evolution – from observations of seismic events.

Generally speaking, the seismicity of a terrestrial planet depends on the state of strain within it. The amount of strain that has accumulated is itself dependent upon the thermal evolution of the planet which is governed by how heat is dissipated. At some point the accumulated strain causes material failure that produces a disturbance which travels from the point of origin through the planet as seismic waves. The disturbances propagate directly to the recording station as P- and S-waves and as reflected and refracted phases that have interacted with the surface (e.g., PP, PPP, SS, and SSS) or internal boundaries such as the core (e.g., ScS). To date (Sol

* Corresponding author at: Institute of Geophysics, ETH Zürich, Zürich, Switzerland.
E-mail address: akhan@ethz.ch (A. Khan).

https://doi.org/10.1016/j.epsl.2021.117330
0012-821X/

864), more than 1000 distinct seismic events have been identified by the Mars Quake Service (MQS) (Clinton et al., 2020), of which a smaller subset has been employed to infer the structure of the crust (Knapmeyer-Endrun et al., 2021), upper mantle (Khan et al., 2021), and core (Stähler et al., 2021).

Existing constraints on the chemical composition of Mars principally derive from meteorites (McSween, 1994; McSween and McLennan, 2014), which rely either on knowledge of their refractory element abundances (Wänke and Dreibus, 1994; Taylor, 2013; Yoshizaki and McDonough, 2020) or their isotopic compositions (Lodders and Fegley, 1997; Mohapatra and Murty, 2003), but invariably require invoking a number of working assumptions (to be discussed in section 2). Both approaches, however, were shown to be fundamentally limited in that they were unable to self-consistently explain major element chemistry and geophysical properties (mean density, moment of inertia and tidal response) simultaneously unless adjustments to, for example, the bulk Fe/Si ratio, core composition, and/or core size were made (Khan et al., 2018; Liebske and Khan, 2019).

Because the mean density of the core trades off with that of the mantle and therefore bulk mantle composition, Khan et al. (2021) and Stähler et al. (2021) considered a number of model Martian compositions (Lodders and Fegley, 1997; Taylor, 2013; Yoshizaki and McDonough, 2020; Khan and Connolly, 2008; Wänke and Dreibus, 1994) as part of the inversion for planetary structure. Their results showed that while core size remained robust, mean core density changed as a consequence of variations in mantle FeO content, ultimately influencing the required proportion of light elements in the core. This, clearly, demands further attention, particularly in view of the importance of core composition as a means of establishing the evolution and differentiation history of Mars, including that of the putative Martian core dynamo that is considered responsible for the ancient strongly magnetised crust observed in the southern highlands (Stevenson, 2001; Mittelholz et al., 2020; Davies and Pommier, 2018).

Relying on a geophysical parameterization that provides an unified description of the mantle and core with petrologic phase equilibria and physical properties as a function of composition, temperature, and pressure, we employ the InSight seismic data, including a set of geophysical observations that sense the large-scale structure of Mars, (described in section 3) to determine mantle and core composition. Following the establishment of geophysically-determined mantle compositions and mean core properties (radius and density), we employ a cosmochemical approach (section 4) by focusing on major elements and the extant correlation between Fe/Si and Fe/Mg that is observed in planetary materials (Yoshizaki and McDonough, 2021). Quantitative comparison of the geophysical and cosmochemical compositions enables us to further restrict the mantle composition of Mars by considering only those compositions that fit both constraints. Finally, we employ the jointly-predicted mantle composition to place constraints on the identities and abundances of light elements in the Martian core (section 6). The novelty of our approach lies in the inversion of multiple geophysical observations to derive physically-credible solutions of the interior state of Mars, in conjunction with cosmochemically-plausible bulk chemical compositions.

2. Previous models of Mars' bulk composition

Early estimates for the composition of Mars were predicated upon cosmochemical arguments, as expounded by Wänke and Dreibus (1994), in which Mars accreted heterogeneously from two components. Initially, they hypothesised, accretion of a highly reduced 'A' component with CI-like abundances for elements more refractory than Mn but devoid of volatiles, is followed by late-stage accretion of oxidised and volatile-rich material with CI-like abundances for the moderately volatile elements as well (termed B), in a ratio of A:B 65:35 (as opposed to 85:15 for the Earth). The key result of these models was the high FeO content of the Martian mantle (∼17–18 wt%) based on the observation that FeO/MnO ratios in Martian meteorites are positively correlated with a slope near unity, combined with the assumption that Mn behaved as a refractory element (component A) during accretion.

The group of Shergottite-Nakhlite-Chassignite (SNC) meteorites are the sole tangible records of the composition of the Martian crust and potentially its mantle. Recently, Yoshizaki and McDonough (2020) used these meteorites, together with surface compositions determined by GRS data (Boynton et al., 2007) to infer the composition of Mars. However, precise determination of the chemistry of the Martian mantle by such an approach is hindered by the fact that there are no extant samples of mantle material in the SNC suite. Rather, lherzolitic- and olivine-rich shergottites represent cumulate rocks of their parental, basaltic melts (McSween, 1994). In fact, when projecting chemical differentiation trends of basaltic and lherzolitic shergottites to a nominal mantle MgO content of 31±2 wt% (Yoshizaki and McDonough (2020), and references therein), the major refractory lithophile elements, Ca and Al, are present in distinctly non-chondritic proportions. That the Ca/Al ratio among shergottites is superchondritic (2.1±0.5) has long been recognised (cf. Agee and Draper (2004)), and likely points to high pressure (≈5 GPa) melt extraction in the presence of a residual aluminous phase, namely garnet. However, Agee and Draper (2004) noted that at such pressures, a Martian mantle composition with ≈18 wt% FeO (cf. Wänke and Dreibus (1994)), would produce FeO contents in parental magmas far in excess (21–30 wt%) of those observed (16–19 wt%). This discrepancy was also noted by Yoshizaki and McDonough (2020), prompting their adoption of an Fe-poorer mantle composition, corresponding to a Mg#=0.79±0.02, which, when combined with an estimated MgO=31±2 wt%, results in FeO=14.7±1 wt%.

These considerations highlight an inherent inconsistency in the direct use of chemical indices of differentiation among shergottites to infer the composition of the Martian mantle. Namely, refractory lithophile elements typically assumed to be present in chondritic ratios (e.g., Y/Ho, Hf/Sc, Gd/Al) in shergottites are no longer so, as they have been fractionated by partial melting processes and subsequent crystal accumulation, thus yielding imprecise information on their degree of enrichment relative to CI chondrites. As such, they cannot be used in a manner analogous to peridotites in Earth's mantle to derive a putative 'primitive mantle' composition.

Although acknowledged to be non-unique, the model of Yoshizaki and McDonough (2020) also features a core that is much too small (radius∼1580 km), even relative to the pre-InSight constraints on radius of 1750–1890 km (Rivoldini et al., 2011; Khan et al., 2018; Bagheri et al., 2019). Despite their careful geochemical approach, the model of Yoshizaki and McDonough (2020) therefore does not simultaneously satisfy major element chemistry and geophysical properties, which we argue is a prerequisite for producing a self-consistent estimate for the composition of Mars, its core, and its mantle.

3. Geophysical constraints on the bulk mantle composition

3.1. InSight seismic and geophysical data

To date (Sol 864), more than 1000 distinct seismic events have been identified (Clinton et al., 2020) that have been classified based on frequency content as either low-frequency (LF) or high-frequency (HF) with energy dominantly below 1 Hz and above 1 Hz, respectively (Clinton et al., 2020; Giardini et al., 2020). Although HF events are much more numerous, these events are believed to represent local disturbances (Dahmen et al., 2021; van

Driel et al., 2021) and provide information on the very near-surface structure (Lognonné et al., 2020). Instead, we rely on 8 of the largest LF events (out of 50) with a high signal-to-noise ratio for which we have been able to make consistent body wave picks as described in detail in Khan et al. (2021) and Stähler et al. (2021). For the events, we have picked the direct P- and S-wave arrivals allowing for distance determination and surface- (PP, PPP, SS, and SSS) and core-reflections (ScS) for interior structure determination. The events were found to occur in the epicentral distance range ∼25°–75° and had moment magnitudes between M_W=3.0–4.0 (Clinton et al., 2020). The back azimuth could only be obtained for three of the events from polarization and were found to be located in the Cerberus Fossae region (Clinton et al., 2020). The differential body wave travel time picks (we reference each pick to the main P-wave arrival) are labelled t_i and summarised in Table A.1. For detailed discussion of the body wave picks, we refer the reader to Khan et al. (2021) and Stähler et al. (2021). Additional information on crustal structure beneath the InSight lander come from receiver functions and auto-correlation of seismic signals (Knapmeyer-Endrun et al., 2021), but are not considered here.

In addition to the seismic data, we consider mean density ($\hat{\rho}$), mean moment of inertia (I/MR^2), and second degree tidal Love number (k_2) that bear directly on the interior structure of Mars (Zharkov and Gudkova, 2005; Khan and Connolly, 2008; Rivoldini et al., 2011; Khan et al., 2018; Bagheri et al., 2019). Mean density and moment of inertia are sensitive to the density structure of the planet, whereas the sensitivity of the second degree tidal Love number is related to the response of the planet to tidal forcing and therefore sensitive to mantle shear modulus and core size. Here, we employ the most recent spacecraft-determined value of k_2=0.174±0.008 by Konopliv et al. (2020), which is considered at the solar period (12h19min). To change to k_2 at seismic periods (∼1 s), consideration of the effect of anelasticity on k_2 to account for the proper frequency dependence is included through the viscoelastic formulation described in Khan et al. (2018), resulting in an elastic k_2 of 0.172±0.008. The geophysical data are summarised in Table A.2.

3.2. Computing geophysical properties

To construct models of the internal structure of Mars, we follow the approach outlined in Khan et al. (2018), where mantle seismic properties (P- and S-wave speeds and density) are computed using petrologic phase-equilibrium computations. For this, we employ Gibbs free-energy minimization (Connolly, 2009), which computes stable mantle mineralogy and physical properties as a function of temperature, composition (in the CFMASNa model chemical system that comprises the oxides CaO-FeO-MgO-Al_2O_3-SiO_2-Na_2O), and pressure based on the thermodynamic formulation and parameters of Stixrude and Lithgow-Bertelloni (2005, 2011). For the crust, we follow Khan et al. (2021) and Stähler et al. (2021), and consider a seismic parameterisation consisting of 3 layers with variable S-wave velocities, P-to-S-wave and density-to-S-wave velocity scaling, and depth nodes.

Martian geotherms are parameterized by a conductive crust and lithosphere underneath which the mantle is assumed to be adiabatic. The conductive part is defined by a linear thermal gradient between the base of the Moho and the base of the lithosphere of variable thickness (Z_{lit}) and temperature (T_{lit}). This assumption implies that no crustal radioactive enrichment is present. Although this is unlikely to be realistic, the exact nature of the crustal geotherm is less important since crustal structure is parameterised in terms of seismic properties. Moreover, the simple linear shape assumed for the entire lithospheric thermal gradient does not imply that there are no radioactive heat sources. A quasi-linear lithospheric thermal gradient is per se not incompatible with the presence of heat producing elements. The implicit assumption here, is that the temperature gradient in the enriched crust and in the depleted lithosphere are the same, whereas differences are expected if the heat producing element content of the two reservoirs are distinct. In summary, what matters is the temperature gradient in the deeper part (below the crust).

Mantle adiabats (isentropes) are computed self-consistently from the entropy of the lithology at the pressure and temperature of the bottom of the lithosphere. Major sources of uncertainty in the thermodynamic calculations are absence of experimental constraints on the parameters relevant for the thermodynamic formalism and parameterization of Stixrude and Lithgow-Bertelloni Stixrude and Lithgow-Bertelloni (2011). Connolly and Khan (2016) estimated the accuracy of the elastic moduli and density to be ∼0.5% and ∼1–2%, respectively. Finally, depth-dependent core properties are computed using an equation-of-state for liquid Fe and liquid Fe-S alloys as described in Appendix B.

The entire forward problem consists in computing differential body wave travel times (Table A.1) and geophysical data (Table A.2) from radial P- and S-wave and density profiles that are obtained from free-energy minimization for a given composition and temperature as described above. Thus the forward problem can be summarized as

$$\{X, T_{lit}, Z_{lit}, Y_{Crust}, R_{core}, \rho_{core}, \Delta, h\} \xrightarrow{g_1} M \xrightarrow{g_2} \{\rho, V_S, V_P\} \xrightarrow{g_3} \{t_i, \bar{\rho}, I/MR^2, k_2\},$$

where the model parameters are summarized in Table C.1 and Y_{Crust} contains the model parameters pertaining to the crust. g_1, g_2, and g_3 represent the forward modelling schemes. The primary parameters are log-uniformly distributed within the wide bounds indicated in Table C.1 that are much larger than InSight mission requirements (e.g., ±5% for S-wave speed). Pressure is computed by integrating the load from the surface boundary condition. This parameterisation differs from that employed in Khan et al. (2021) and Stähler et al. (2021) in one important aspect – by considering mantle composition (X) as a model parameter as in our previous work (Khan and Connolly, 2008). To solve the inverse problem posited here, we make use of the probabilistic approach of Mosegaard and Tarantola (1995), which is described in appendix C. As part of the stochastic inversion method, it is usual practice to start with different initial models (here bulk mantle composition and areotherm) to ensure sufficient coverage of the model space while sampling. For this, we commenced with five different "high FeO" models (FeO>17 wt%) and areotherms that varied within a range of 150 K.

3.3. Bulk mantle compositions

Based on this inversion scheme, we inverted the differential travel times (Table A.1) jointly with the geophysical data (Table A.2) for the primary parameters listed in Table C.1. In the following, we focus on thermo-chemical parameters and leave geophysical properties aside (sampled areotherms are shown in Fig. D.1). Inverted mantle compositions in the form of major element distributions (we focus on the oxides of Fe, Mg, and Si), core properties (radius and mean density), and mantle potential temperature are shown in Fig. 1. The minor elements (Al, Ca and Na) are also varied but the geophysical data are less sensitive to variation in their abundances. From the major element distributions (Fig. 1A), we make the following observations: 1) mantle FeO content varies in the range 12.5–15 wt%; 2) a lower mantle FeO content generally correlates with a lower MgO and higher SiO_2 content. From the inverted core properties (Fig. 1B), we see that 3) a higher mean core density correlates, as expected, with a smaller

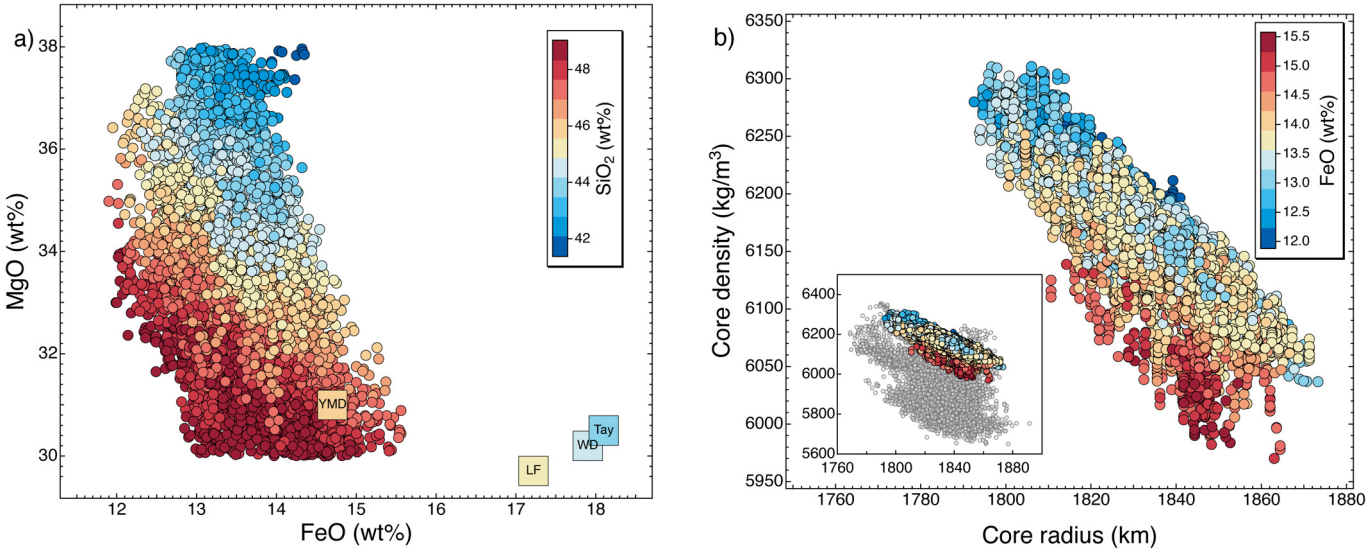

Fig. 1. Inverted mantle compositions and core properties. (a) FeO, MgO, and SiO_2 distributions obtained from inversion of geophysical data. Squares indicate earlier bulk mantle compositions (WD–Wänke and Dreibus (1994); LF–Lodders and Fegley (1997); TAY–Taylor (2013); YMD–Yoshizaki and McDonough (2020)). (b) Mean core density as a function of core radius and mantle FeO content. Inset shows comparison with the results from Stähler et al. (2021) (grey circles). (For interpretation of the colours in the figure(s), the reader is referred to the web version of this article.)

core radius; and 4) the inverted core radii and mean core densities span the ranges from 1790 km to 1870 km and 6000 kg/m^3 to 6300 kg/m^3, respectively. The radius range of the liquid core found here is largely consistent with that obtained by Stähler et al. (2021) of 1790–1870 km (see inset Fig. 1B), whereas the present core density range covers and extends the upper part of the range found in Stähler et al. (2021) of 5700–6300 kg/m^3, as a consequence of the lower mantle FeO content of the present models relative to what Stähler et al. (2021) considered.

Fig. 1 shows clearly that irrespective of compositional starting model, the inverted compositions, i.e., those fitting the geophysical observations, all converge upon FeO contents <15 wt%. Thus, the mantle FeO content of the Martian mantle is significantly lower than has been predicted in the "canonical" models (Wänke and Dreibus, 1994; Lodders and Fegley, 1997; Taylor, 2013) (Fig. 1A) and its enrichment relative to that of Earth's is less pronounced than initially thought. With these observations, earlier geochemical models that pointed to Mars' mantle containing less FeO (Agee and Draper, 2004; Yoshizaki and McDonough, 2020) are put on a quantitative footing. This had already been suggested in Stähler et al. (2021) based on the fixed bulk Mars compositions considered therein, since unreasonably large amounts of light elements dissolved in the core would be required for mantle FeO contents that exceed ∼16 wt%.

As part of our calculations, we have assumed the mantle of Mars to be compositionally uniform. Yet, Mars likely underwent early magma ocean crystallisation and solidification that could have resulted in compositionally distinct mantle reservoirs with variable FeO content (e.g., Elkins-Tanton et al., 2003; Samuel et al., 2021). Gamma-ray spectrometer data also indicate variations in surface FeO content with the northern plains having higher FeO than the southern highlands (Boynton et al., 2007; Rogers and Hamilton, 2015) and a similar non-uniformity for K and Th (Taylor et al., 2007). These variations could reflect surface processes but may also originate from variability in mantle chemistry. More specifically, the chemical diversity in Fe/Mg and trace element ratios among shergottites imply variations in either their mantle source regions or in the amount of partial melting (McSween and McLennan, 2014). Current seismic observations, however, are unable to distinguish between a homogeneous and a heterogeneous Martian mantle. Consequently, the model compositions presented here represent integrated mean values.

To further narrow the range of plausible geophysically-derived compositions presented here, independent constraints are needed. To do so, we generate a set of mantle compositions that are obtained from an independent cosmochemical model (to be discussed in the next section), which we subsequently compare to the geophysically-based compositions using a quantitative measure. This procedure allows us to significantly refine estimates of the mantle composition of Mars.

4. Cosmochemical constraints on mantle and core compositions of Mars

Given the difficulty of using SNCs to derive the Martian mantle composition (see section 2), here we employ a cosmochemical approach to place constraints on the mantle composition of Mars. Following the geophysical approach, where the crust is parameterised purely in terms of seismic properties, we neglect compositional variability in this layer. We instead concentrate our efforts on the five major oxides, SiO_2, MgO, FeO, Al_2O_3 and CaO, that, in descending order, together comprise ∼98.5% (by weight) of the rock-forming elements of the Earth's mantle (cf. Palme and O'Neill (2014)) and ∼98 % of previous estimates for Martian compositions (Wänke and Dreibus, 1994; Taylor, 2013; Yoshizaki and McDonough, 2020). As such, they are most likely to account for the vast majority of the variability in seismic wave velocities in Mars' mantle (e.g., Khan and Connolly, 2008). Because the geophysical inversions consider six oxides which must sum to 100 %, we presume the five major oxides sum to 99±0.5%, with the remainder being Na_2O (this implicitly ignores the presence of minor oxides, chiefly TiO_2, Cr_2O_3 and MnO, which together total ∼0.5 to 1 wt%). We adopt this observation as the first constraint to ensure consistency between the geophysical and the cosmochemical models (in wt%)

$$SiO_2 + MgO + FeO + Al_2O_3 + CaO = 99 \pm 0.5, \quad (1)$$

Of these, Ca and Al are refractory lithophile elements (RLEs), whose significance lies in the fact that they are neither fractionated by

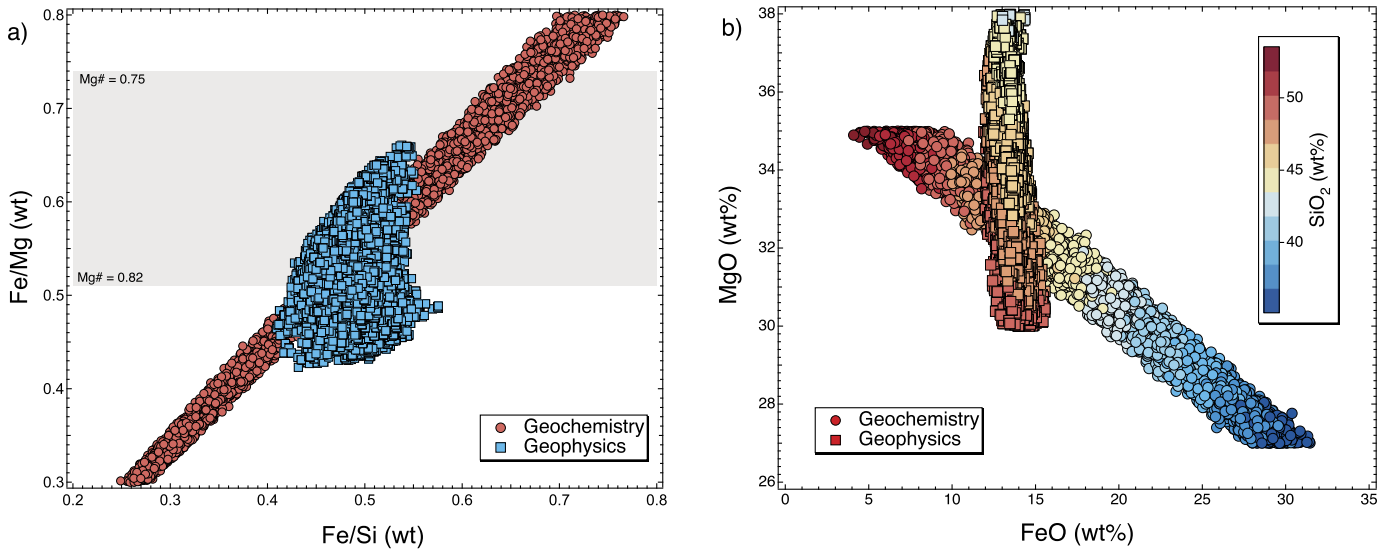

Fig. 2. Comparison of geophysical and cosmochemical model compositions. (a) Distribution of Fe/Mg versus Fe/Si (wt) for the geophysically-inverted compositions and the predicted compositions from the cosmochemical model (based on 10000 model predictions). Note that only a limited range of the cosmochemical models are shown. Grey bar represents the range of mantle Mg# based on petrological estimates from the literature (e.g. Collinet et al., 2015). (b) Same as (a) but for MgO, FeO, and SiO_2. See main text for details.

volatility-related processes during planetary formation (e.g., O'Neill and Palme, 1998), nor are they appreciably sequestered into the Fe-Ni-rich metallic cores of rocky bodies. Therefore, one can place a minimum bound on the abundances of Ca and Al in a planetary mantle by considering their concentrations in chondritic meteorites and the mass fraction of its core. Given an ordinary chondrite-like bulk composition with CaO = 1.84 wt% and Al_2O_3 = 2.25 wt% (Wasson and Kallemeyn, 1988), and a Martian core mass of 25 ± 0.5% based on Stähler et al. (2021) and this study, then, CaO = 2.45 wt% and Al_2O_3 = 3.00 wt%, which are identical to the Wänke and Dreibus (1994) and Taylor (2013) models, and slightly lower than the estimates of Yoshizaki and McDonough (2020), who give CaO = 2.88 wt% and Al_2O_3 = 3.59 wt%. Taking an average of these estimates, we impose the second constraint, which is (in wt%)

$$Al_2O_3 + CaO = 6.1 \pm 1.0, \quad (2)$$

and given that the chondritic Ca/Al ratio is 1.08 ± 0.02 (Wasson and Kallemeyn, 1988), the corresponding oxide ratio becomes

$$CaO/Al_2O_3 = 0.81 \pm 0.02, \quad (3)$$

The three remaining oxides, SiO_2 + MgO + FeO therefore constitute 92.9 ± 1.5 wt% of the mass of the mantle. Furthermore, all three condense from a cooling solar nebula gas near 1330 K into olivine (MgO and SiO_2) and metal (Fe). Yoshizaki and McDonough (2021) noted the positive correlation between Fe/Si and Fe/Mg ratios in planetary materials ($r^2 = 0.88$), in particular defined by chondritic meteorites (ordinary, carbonaceous and enstatite, excepting EH-type). Bulk Earth and Mars are also thought to lie on the correlation based on chemical trends in peridotites and shergottites, respectively (cf. Figure 1 in Yoshizaki and McDonough (2021)), which yields

$$Fe/Mg_{\bigcirc} = 0.835 \times Fe/Si_{\bigcirc} + 0.460, \quad (4)$$

where ○ refers to the bulk planet and the uncertainty on the numbers are ±0.007 and ±0.01, respectively. Mechanistically, this correlation arises due to differences in the metal/silicate ratio of the bulk meteorite. The observed slope of 0.835, given a Mg# (molar $Mg/(Mg+Fe^{2+})$ ratio in silicates of 0.86 (O'Neill and Palme, 1998), is consistent with a binary mixture of Fe-rich metal and a second component with 62% olivine and 37% orthopyroxene, reflecting the ratio at which these two phases condensed from the solar nebula. Although this correlation is defined chiefly by chondrites, it does not require the building blocks of Mars to have been chondritic (Liebske and Khan, 2019). Instead, components with Fe/Mg and Fe/Si ratios outside those of the existing range of chondrites are permitted, provided they adhere to Eq. (4). Moreover, because the stable isotopic ratios of Mg, Fe and Si are fractionated to < 1/10000 in the Earth and Mars relative to chondritic meteorites (Sossi et al., 2016; Hin et al., 2017), their losses by volatility-related processes on a planetary scale were limited, meaning the bulk compositions, even of differentiated bodies, should follow the same Fe/Si vs. Fe/Mg trend. This assertion is further supported by two independent observations: *i*) the composition of the bulk Earth lies on the trend defined by chondrites and *ii*) the geophysically-determined mantle compositions derived here overlap with those derived cosmochemically, given a core mass fraction of 0.25 (Fig. 2). On this basis, we propose that the bulk composition of Mars also lies within the uncertainty of the Fe/Mg–Fe/Si correlation defined by planetary materials.

Importantly, Mg and Si are also lithophile elements, meaning their abundances in Mars' core are negligible with respect to those in the mantle. Although Si can become siderophile at very low fO_2 and at high pressures and temperatures (Fischer et al., 2015), these conditions are unlikely to have prevailed during the formation of the Martian core (cf. section 6). Therefore, for the purpose of this exercise, it is reasonable to assume that the Mg/Si ratio of the Martian mantle is equivalent to that given by Eq. (4) for the entire planet, thus

$$Mg/Si_{\oplus} = Mg/Si_{\bigcirc}, \quad (5)$$

where ⊕ refers to the mantle part of the planet. In order to calculate cosmochemically-plausible Martian mantle compositions, given the above constraints, the bulk Fe content of Mars and the MgO content of its mantle are kept as free parameters. Because the Mg/Si ratio constrains the SiO_2 content for a given mantle MgO content (Eq. (5)), the FeO content of the mantle is uniquely given by (in wt%)

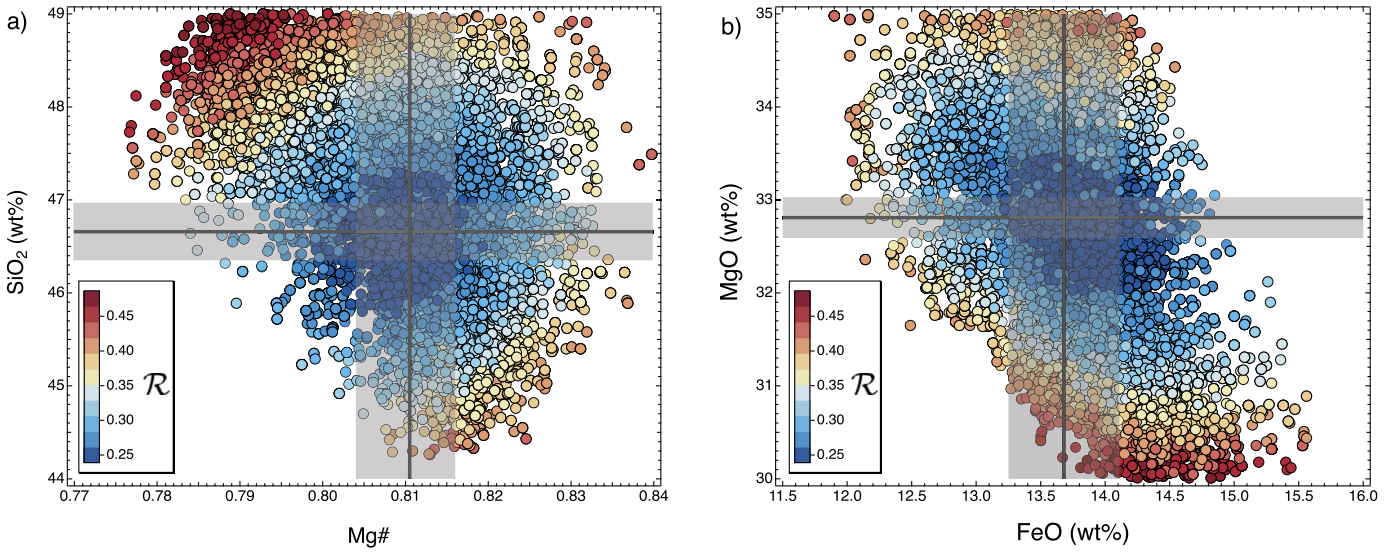

Fig. 3. Major element composition of the Martian mantle. The distributions of (a) SiO_2 versus Mg# and (b) MgO versus FeO are colour-coded for their average root-mean-squared difference ($\mathcal{R}$) between the geophysically-derived and the cosmochemically-plausible synthetic compositions. Blue points represent the lowest deviation and therefore the most probable compositions.

$$FeO_{\oplus} = 92.9 - MgO - SiO_2, \quad (6)$$

where the uncertainty on the first number is ±1.5 wt%. Assuming the Fe/Si–Fe/Mg trend provided by the meteoritic record with the exception of the EH chondrites (Yoshizaki and McDonough, 2021), this set of 6 equations and 5 unknowns (FeO, MgO, SiO_2, Al_2O_3, and CaO) can be used as a recipe to determine the mantle composition of any rocky body. Furthermore, as the Fe content of bulk Mars is specified as an input parameter, the Fe content of the core is determined by mass balance

$$f_{\odot} \cdot Fe_{\odot} = Fe_{\bigcirc} - Fe_{\oplus} \times (1 - f_{\odot}), \quad (7)$$

where the subscript $\odot$ refers to the core of the planet and $f_{\odot}$ refers to core fraction. Given this general framework, a Monte Carlo model is developed in which the MgO content of the mantle is selected from a uniform distribution between 27 and 35 wt% and the bulk Fe content from between 26 and 30 wt%. The simulation is then performed for 10^4 iterations in order to produce synthetic Martian mantle compositions and core Fe contents, in which the parameters in Eqs. (1) through (7) are selected from a uniform distribution within their uncertainties. The results are shown in Fig. 2. The grey bar comprises the range of literature estimates of Mg# based on Martian igneous rocks (Collinet et al., 2015).

The compositional range is, owing to the positive slope of the Fe/Mg–Fe/Si trend (Fig. 2A), defined by a marked negative correlation between the MgO and FeO abundances in the mantle (Fig. 2B), which precludes mantle compositions lying in the Fe, Mg-rich or Fe, Mg-poor quadrants of Fig. 2A. The slope of the trend also dictates that silica-rich mantles only occur in high MgO, low FeO compositions, and vice-versa.

5. Composition of the Martian mantle from geophysical and cosmochemical constraints

The geophysical and cosmochemical models derived above represent two independent estimates of the composition of the Martian mantle and core. In order to garner more precise estimates that are compatible with both models, we construct matrices containing both the synthetic and geophysically-inverted mantle compositions of the five major oxides to quantitatively assess the mean misfit (here denoted $\mathcal{R}$) of the geophysical compositions from their cosmochemical counterparts. Numerically, this is described by the following relation

$$\mathcal{R}_k = \sum_i \sum_j \sqrt{\frac{[X_c^j - X_g^j]^2}{\alpha N_g}} \quad (8)$$

where X_c and X_g are the weight percentages of each oxide in the cosmochemical and geophysical models, respectively, N_g is the number of geophysical models, i the number of synthetic cosmochemically-derived compositions, and j is any of the 5 major oxides considered here. Therefore, a χ^2-misfit value is computed for each geophysical model k according to the deviation from each of the 10^4 cosmochemical compositions across the five oxides. Dividing this value by the number of oxides (α=5) and the number of geophysical models yields the root-mean-squared misfit ($\mathcal{R}$) per oxide per model.

This information, for a subset of geophysical models with MgO between 30 and 35 wt%, is plotted in Fig. 3, in which $\mathcal{R}$ ranges from 0.24 to 0.5. Importantly, the minimum (i.e., best-fitting) values are concentrated in a narrow band of MgO contents between 32.5 and 33 wt%, while FeO values below 12.5 wt% are precluded by both cosmochemical and geophysical constraints. As is evident from Fig. 3, MgO values that are too low or too high imply FeO values that are too high or too low, respectively, with respect to the geophysical inversions and are thus implausible. These low $\mathcal{R}$ values correspond to Martian mantle silica contents of 46 to 47 wt%.

In order to derive a precise estimate for the composition of the Martian mantle, we filter the geophysical inversions by the top 2.5% of the $\mathcal{R}$ values, mirroring 2 standard deviations about the mean (although the $\mathcal{R}$ values are not normally distributed). This corresponds to 938 geophysical models, the results of which are summarised in Table 1.

The FeO content is ∼1 wt% lower than that derived by Yoshizaki and McDonough (2020) and the MgO content almost 2 wt% higher. Together, they yield an Mg # of the Martian mantle of 81±0.5, consistent with petrologically-derived estimates (cf. Agee and Draper (2004)). The principal differences in the Martian mantle composition compared with that of Yoshizaki and McDonough (2020) can be ascribed to the fact that we adopt the much larger core mass of 0.25 ($R_{\odot}$ = 1840 km) compared to that used in Yoshizaki and McDonough (2020) of 0.18 ($R_{\odot}$ = 1580 km).

Table 1
Best-fit average values of the Martian mantle composition in the system CFMASNa (normalised to 100%, see section 4), potential temperature, and core ($\odot$) properties based on the 2.5 % of the population of geophysical models with the lowest $\mathcal{R}$ with respect to cosmochemical estimates (resulting in 938 out of 10^4 models). The core Fe content ($Fe_\odot$) is calculated using eq. (7).

Property	SiO_2	Al_2O_3	MgO	CaO	FeO	Na_2O	T_{pot} (K)	$R_\odot$ (km)	$\rho_\odot$ (kg/m^3)	$Fe_\odot$
Average	46.66	3.49	32.81	2.66	13.68	0.69	1635	1836	6150	81.6
1-σ	0.31	0.15	0.22	0.17	0.43	0.16	31	11	46	3.8

Table 2
Estimates of the abundances of moderately volatile lithophile elements in the Martian mantle based on lherzolitic and olivine-phyric shergottites. YMD refers to Yoshizaki and McDonough (2020). Major differences between this work and YMD for Zn, Mn and Na relate to the choice of normalising element. Alternatively, using the constancy of Fe/Zn and Fe/Mn ratios in shergottites, $2.1\pm0.3\cdot10^{-5}$ and 38.1±3.1, respectively, one obtains 51±7 ppm for Zn and 2795±225 ppm for Mn given FeO = 13.7 wt%.

Element	Element Ratio	Concentration (this work) (ppm)	Concentration (YMD) (ppm)
Zn	Avg. Shergottites	65.9±8.5	45±15
Mn	Avg. Shergottites	3681±387	2880±518
In	In/Y	0.012±0.003	0.01±0.005
Tl	Tl/Sm	0.006±0.002	0.004±0.002
Ga	Ga/Al	9.7±1.0	8.7±1.9
Li	Li/Yb	1.78±0.32	1.8±0.4
Na	Na/Yb	2739±387	4300±964
K	K/La	468±74	360±40
Rb	Rb/La	1.23±0.19	1.2±0.4
Cs	Rb/Cs = 15.5±9.2	0.08±0.03	0.07±0.03

Accordingly, our estimates for the FeO content of the Martian mantle are lower, and those for MgO contents higher, than Yoshizaki and McDonough (2020) in order to satisfy Mars' moment of inertia, Love number, and larger core mass evidenced by seismic reflections occurring at ∼1540 km below the Martian surface as recorded by the InSight mission.

Should T_{pot} have been overestimated, then this would only drive mantle FeO contents to lower values, because increasing temperature or decreasing FeO content both conspire to decrease seismic velocities. A similar trade-off is observed between the FeO content of the mantle and its mean density and radius (Fig. 1). Specifically, lower FeO contents would result in higher core densities and smaller core radii. The mean density of the core by using the cosmochemically-constrained subset of the geophysical models is 6304±38 kg/m^3, while its Fe content is 81.6±3.8 wt% (from Eq. (7)), the implications of which are discussed in the next section.

6. Constraints on light elements in the Martian core

6.1. Volatile elements and the S content of Mars

Because volatile elements are not uniformly abundant among different chondrite groups, their concentrations in bulk Mars are better constrained through direct measurement of SNC meteorites. While the uncertainty in the degree of RLE enrichment in the Martian mantle (a factor of ≤ 2; Taylor (2013), and references therein), when propagated to the abundances of major elements, is significant, this is not so for volatile trace elements, because their abundances tend to vary by orders of magnitude. Therefore, the SNC meteorites remain the most faithful probes of the composition of the Martian mantle with respect to volatiles.

The importance of understanding the depletion of volatile elements in Mars lies in their potential to constrain the abundances of volatile chalcophile or siderophile elements that may have partially entered the Martian core. To do so, only the concentrations of lithophile (or weakly siderophile) elements in lherzolitic and olivine-phyric shergottites are examined. Their concentrations are then divided by that of a refractory element with equivalent compatibility during partial melting on Mars. In this manner, the effect of partial melting is normalised out of the equation, and the nominal mantle abundance of a given volatile element is returned. Element ratios used for this exercise are listed in Table 2, while for elements with partition coefficients of unity (Zn and Mn; (Davis et al., 2013)), their average abundances or normalisation to Fe in the shergottites can be used.

Once determined, the abundance of a given element in the Martian mantle is double-normalised by its abundance in CI chondrites (Palme and O'Neill, 2014) and by Al to give the depletion factor

$$f(x) = \frac{[x/\mathrm{Al}]_\oplus}{[x/\mathrm{Al}]_{\mathrm{CI}}}, \tag{9}$$

where x is any of the elements in Table 2 and the ratios refer to those in the Martian mantle ($\oplus$) and the CI chondrites, respectively. Comparing the depletion factor of element x to its 50 % nebular condensation temperature (T_c), permits the definition of 'volatile depletion trends' among lithophile elements in the Martian mantle (Fig. 4). These trends can be fit by logistic functions

$$f(x) = \frac{1}{1+\exp[-k(T_c - T_0)]}, \tag{10}$$

where k is the steepness of the logistic curve, and T_0 its inflection temperature. Fits of Eq. (10) to the Martian mantle abundance data (Table 2) yield k = 0.0071±0.0015 K^{-1} and T_0 = 1020±27 K for the values derived herein, and k = 0.0060±0.0008 K^{-1} and T_0 = 1049±20 K using the data of Yoshizaki and McDonough (2020). If the condensation temperatures from Wood et al. (2019) are used instead, then k = 0.0053±0.0017 K^{-1} and T_0 = 1030±48 K using our data, and k = 0.0051±0.0010 K^{-1} and T_0 = 1059±18 K with the data of Yoshizaki and McDonough (2020).

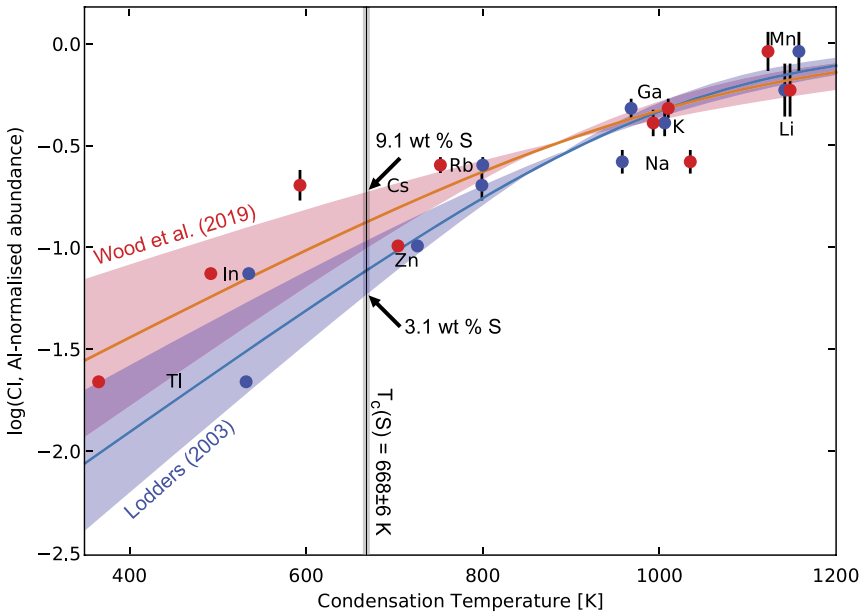

Fig. 4. Volatile depletion trend of the Martian mantle defined by the CI- and Al-normalised abundances of moderately volatile lithophile elements (coloured points, Table 2, this study) according to the T_c values of Lodders (2003) (blue) and of Wood et al. (2019) (red). The data are fit according to logistic curves (Eq. (10)) and shown along with their 1-σ error envelopes. The vertical line represents the condensation temperature of S, and its intersection with the logistic curves corresponds to the minimum and maximum core S contents listed.

These functions and their associated uncertainties permit estimation of bulk Mars' S content through interpolation (eq. (10)) to yield $f(S)$ given its nebular condensation temperature of 668±6 K (Lodders, 2003; Wood et al., 2019). Then, using the Al contents of CI chondrites (Al_{CI} = 8400 ppm) and the Martian mantle ($Al_{\oplus}$ = 18712 ppm or 3.5 wt % Al_2O_3) and its core mass fraction ($f_{\odot}$ = 0.25), the S content in the Martian core is

$$S_{\odot} = \frac{\frac{S_{CI}}{Al_{CI}} \times Al_{\oplus} \times f(S)}{f_{\odot}}, \quad (11)$$

yielding values of $3.7^{+1.4}_{-0.6}$ wt% and $4.5^{+1.0}_{-0.7}$ wt% using the volatile abundances determined here and by Yoshizaki and McDonough (2020), respectively. However, the derivation of S abundances in the core is sensitive to the choice of condensation temperatures of volatile lithophile trace elements with T_c close to that of S, and their T_c have been revised downward in Wood et al. (2019) relative to Lodders (2003). Using the T_c of Wood et al. (2019), S contents are revised upwards to $6.2^{+2.9}_{-1.4}$ wt% (this work) and $5.7^{+1.5}_{-1.0}$ wt% for Yoshizaki and McDonough (2020). To reach the ∼ 15 wt % S proposed in earlier models (Wänke and Dreibus, 1994) requires a bulk Martian S content of 3.75 wt% ($\log_{10}[f(S)]$ = -0.5), exceeding the range of all chondrites except CI and EH. However, owing to the considerable uncertainty in the condensation temperatures and elemental abundances, it is not inconceivable that the Martian core contains up to ∼9 wt% S, falling within the range of earlier predictions (Wang and Becker, 2017; Steenstra and van Westrenen, 2018).

6.2. Core composition models for Mars

The combined geophysical and cosmochemical constraints suggest a mean core density around 6150 kg/m^3, requiring a significant complement of light elements in the Martian core, of which S, C, O, and H appear most plausible (Taylor, 2013; Yoshizaki and McDonough, 2020). Previous studies have attempted to estimate the composition of the Martian core either from predominantly bulk geochemical constraints (e.g. Wänke and Dreibus, 1994; Lodders and Fegley, 1997; Taylor, 2013; Yoshizaki and McDonough, 2020) and/or metal-silicate partitioning data (Rubie et al., 2004; Steenstra and van Westrenen, 2018; Brennan et al., 2020).

In order to assess the extent to which a given element enters (and remains in) the Martian core such that it contributes to the observed density deficit, three important considerations are outlined. The extent of element dissolution in the core with respect to the mantle is governed by its partition coefficient, D, defined as the concentration ratio of the element of interest in metal and silicate, respectively. Combined with the core mass fraction and expected budget of the element in the bulk planet, this parameter permits calculation of the amount of an element present in the core. The D value is a complex function of pressure, temperature and composition, while the accretion path undergone (Rubie et al., 2015), the equilibration degree (Rudge et al., 2010) and material accreted by the planet (Ricolleau et al., 2011) also influence the ultimate composition of the core. Due to the degenerate nature of the problem, in this work we seek only to place upper limits on element concentrations in the core. Secondly, for volatile elements, namely C and H, their availability at the core-mantle interface is also limited by their solubility in the magma ocean, as controlled by the vapour pressures of carbon- and hydrogen-bearing species (e.g., CO, CO_2, H_2, H_2O, and CH_4) in the proto-atmosphere (Hirschmann, 2016). Relative to C and H concentrations in chondrites, additional atmospheric losses and/or catastrophic "blow-off" on planetesimals may therefore further lower their overall complement in the silicate reservoir. Lastly, the assumption that elements, once partitioned between core and mantle reservoirs, remain isolated without subsequently back-reacting with the solidified silicate, is uncertain for highly volatile and mobile species such as H (Shibazaki et al., 2009).

In this section, we review solubilities and metal-silicate partitioning of potential light elements in the Martian core. The aim is not to derive a unique core composition, but rather to define likely combinations of light elements (S, C, O, and H) that fit the observed mean core density. Owing to the oxidised nature of the Martian mantle, Si is not likely to be present in appreciable amounts in the Martian core and is omitted here (see Steenstra and van Westrenen, 2018; Brennan et al., 2020, for detailed discussion).

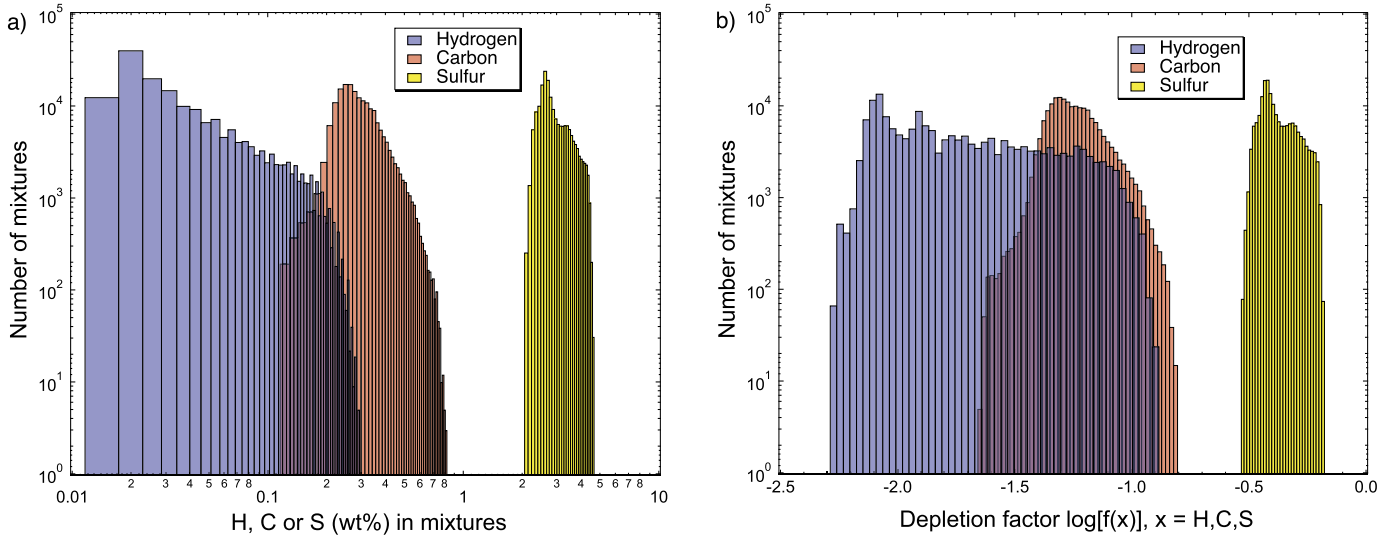

Fig. 5. Light element concentrations in planetary materials. (a) Hydrogen, carbon, and sulfur concentration histograms of 185257 mixtures of chondrites and achondrites consistent with the isotopic signature of Mars (from Liebske and Khan, 2019). The maximum values are considered as upper limit for the abundance of the element of interest during core formation. (b) CI- and Al-normalized depletion factors according to Eq. (9) for the weight distributions shown in (a). See text for details.

6.2.1. Alloying elements I: nickel and cobalt

Before considering the light elements, we establish the probable concentrations of both Ni and Co in the core. As argued above, geochemical and geophysical constraints point to a bulk planet Fe concentration of ∼28.5 wt%, with a core Fe content of 81.6±3.8 wt%. Compositional trends in meteorites (Wasson and Kallemeyn, 1988) show a well-defined linear relationship between Ni and Co versus bulk Fe (in wt%) with correlation coefficients of 0.978 and 0.966, respectively, such that

$$\mathrm{Ni} = -0.13678(\pm 0.0839) + 0.06366(\pm 0.00362) \times \mathrm{Fe} \quad (12)$$

$$\mathrm{Co} = -0.00877(\pm 0.0053) + 0.00321(\pm 0.00023) \times \mathrm{Fe} \quad (13)$$

Adopting the silicate mantle concentrations of Ni and Co proposed by Yoshizaki and McDonough (2020) of 460±120 ppm and 96±44 ppm, respectively, we obtain core concentrations of 6.6±0.9 wt% for Ni and 0.22±0.1 wt% for Co. Thus, with ≈9 wt% S (section 6.1), this implies that Fe, S, Ni, and Co account for ⩽97.4 wt% of the core.

6.2.2. Alloying elements II: hydrogen, carbon and oxygen

Hydrogen, carbon, and oxygen are, next to sulfur, the most abundant elements expected to influence the mean core density. The concentrations of O in the core may be estimated directly from partitioning data if core formation conditions are known, as O is a major element in the mantle and therefore, dissolution in core melts is not limited by its overall abundance. The concentrations of C and H in core-forming liquids are poorly constrained owing to their variable abundances in chondrites, and because their degassing and/or late addition post core formation may obscure any signatures of core-mantle equilibrium (e.g., Hirschmann, 2016).

Because estimating planetary abundances of C and H using volatility, as done for S (section 6.1), is not meaningful on account of their very low condensation temperatures, we consider chondrites and achondrites as potential planetary building blocks and their C and H contents as proxies for the maximum plausible element concentrations that can be acquired during accretion. Liebske and Khan (2019) determined a large range of mixtures of differentiated and undifferentiated objects that are consistent with the isotopic signatures of SNC meteorites and global-scale geophysical data for Mars. Here, we use the isotopically-valid mixtures of Liebske and Khan (2019) to determine their C and H abundances (Fig. 5). We assign 100 ppm hydrogen to both enstatite and ordinary chondrites (e.g. Vacher et al., 2020) and 1000 ppm C and H to the Angrite Parent Body and the Eucrite Parent Body. The result of this estimation is not critically dependent on these values, because the maximum abundances of C and H are predominantly determined by the amount of carbonaceous material, in particular CI and CM, in such mixtures. We included S in this analysis as it provides a reference to the estimated depletion relative to CI and Al Fig. 4.

Fig. 5 shows histograms of the weight fractions of H, C, and S for those chondrite and achondrite mixtures that are isotopically consistent with Mars, and the corresponding CI- and Al-normalized depletion factors calculated from Eq. (9). Sulfur is more depleted in Mars with a minimum depletion factor of $\log_{10}[f(S)]$ = -0.7 (cf. Fig. 4), relative to the sum of potential building blocks with a minimum $\log_{10}[f(S)]$ = -0.5. This discrepancy likely reflects volatile depletion occurring during accretion. The maximum concentrations of both C and H in bulk Mars (Fig. 5), of 0.82 wt% and 0.29 wt% with corresponding depletion factors of $\log_{10}[f(C)]$ = -0.81 and $\log_{10}[f(H)]$ = -0.89, respectively, therefore only serve as theoretical maximum estimates for the element abundances available during core formation.

Carbon is siderophile, with partition coefficients between silicate and metallic melts ranging from $\sim 10^{1}$ to $\sim 10^{3.5}$ (e.g. Dasgupta et al., 2013; Dalou et al., 2017; Tsuno et al., 2018; Malavergne et al., 2019; Fichtner et al., 2021). Our approach is to assume that all C partitions into the core to provide an upper bound. With a core mass fraction of 0.25 and the maximum carbon content of the mixtures (Fig. 5), we obtain an upper limit on C in the core of 3.3 wt%, neglecting any losses due to volatilization or magma ocean degassing. We also note that the solubility-limit of carbon is dependent of the S concentration of the alloy, and for ≈9 wt% S, carbon concentrations of 2–3 wt% in the alloy are feasible before graphite or diamond precipitation occurs (Tsuno et al., 2018; Steenstra and van Westrenen, 2018).

Oxygen partitioning experiments between core-forming metallic liquids and solid or liquid silicate show that its solubility in metal increases with temperature and the activity of FeO in the silicate (e.g. O'Neill et al., 1998; Rubie et al., 2004; Asahara et al., 2007; Ricolleau et al., 2011). The highest O concentrations in the Martian core therefore result from a hot magma ocean extending to the core-mantle-boundary. For bulk mantle FeO concen-

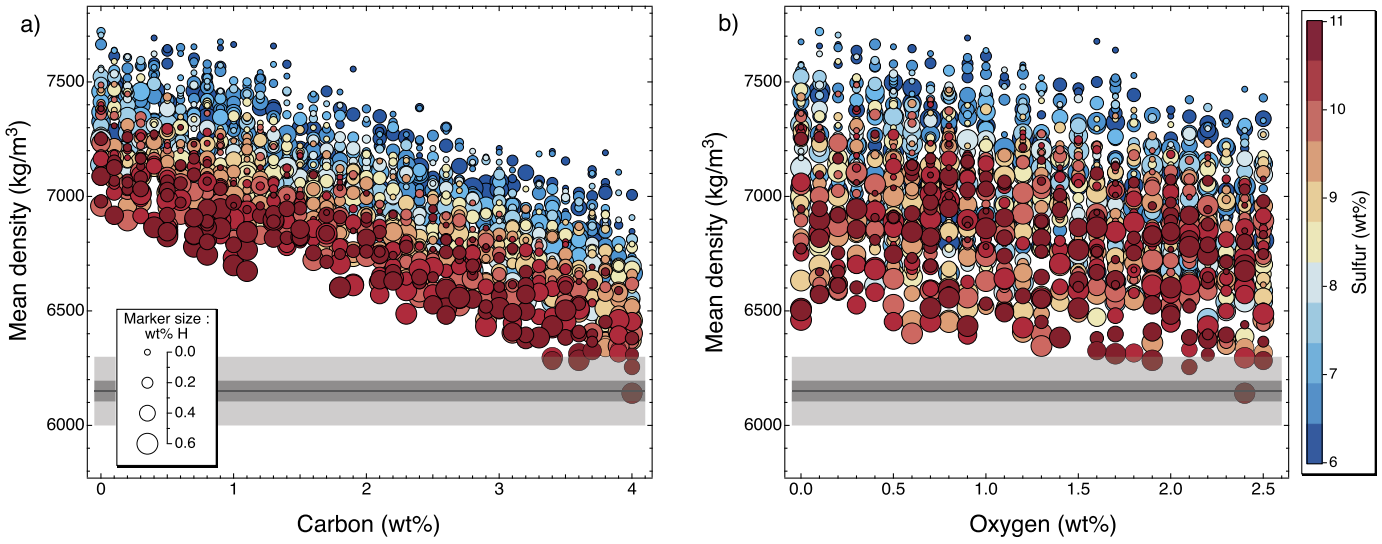

Fig. 6. Variation in mean core density with composition. (a) shows the impact of variations in carbon, sulfur, and hydrogen content on mean core density, while (b) shows the same for variations in oxygen, sulfur, and hydrogen content. Light grey bars indicate the range of geophysically-determined mean core density (cf. Fig. 1b), whereas the black lines and dark grey bars represent the joint geophysical-cosmochemical predicted mean core density (cf. Table 1).

trations between 17–18 wt% (Wänke and Dreibus, 1994; Lodders and Fegley, 1997) and an equilibration pressure of 20 GPa, Steenstra and van Westrenen (2018) estimated the O content to be no more than 4 wt%. This maximum O concentration decreases with lower metal-silicate equilibration pressures and temperatures, and is further lowered for mantle FeO of ∼13–14 wt% as derived here. Correcting the estimate of Steenstra and van Westrenen (2018) to this mantle FeO content and a core-mantle-boundary pressure of 18–19 GPa (T∼2300 K), results in a maximum oxygen content of ⩽2 wt%.

While early studies of the partitioning of H between metal and silicate showed high solubility of H in metal (Okuchi, 1997), more recent studies (Clesi et al., 2018; Malavergne et al., 2019), with bulk H_2O concentrations more appropriate for terrestrial mantles, found that H behaves as a lithophile element (i.e., with $D^{metal/silicate}$ ∼0.1–0.01). The D_H value shows a positive pressure dependence, implying siderophile behaviour at pressures near that of the present-day core-mantle-boundary of Mars ∼19 GPa (this study). The influence of other parameters, such as temperature, silicate or alloying compositions are less well-known. Based on a multi-stage core-formation model, Clesi et al. (2018) obtained ∼60 ppm H in the Martian core, whereas the parameterization of Malavergne et al. (2019) for a single-stage core-formation model at core-mantle-boundary pressures, would allow for much higher concentrations of hydrogen in the core.

Because hydrogen may potentially become siderophile at higher pressures, and core-formation conditions are not precisely known, we evaluate the effect of different D values assuming a bulk concentration of 0.29 wt% H (Fig. E.1). For this H content, we obtain ∼0.3 wt% H in the core, should it have formed in a single-stage event at 19 GPa, for which D≈1 appears possible (Clesi et al., 2018; Malavergne et al., 2019). Simultaneously, the magma ocean must be able to maintain a dissolved equivalent of 3 wt% H_2O. Higher H concentrations in core liquids would require partition coefficients that are unrealistic for Mars.

7. Discussion

7.1. Implications for core composition

To assess the geophysical feasibility of the core compositions derived in the previous section, we generated a set of 10^4 core

Table 3
Upper limits on possible light elements in the core. Values for C and H assume no loss due to volatility or degassing. O and H concentrations require metal-silicate equilibration in the vicinity of present-day core-mantle-boundary temperatures. All numbers in wt%.

Element	S	C	O	H
Upper limit	≈9	⩾3	⩽2.5	⩽0.5

composition models by randomly varying abundances of Fe (including Ni and Co), S, C, O, and H. The sum of Fe+Ni+Co was varied within the geophysically and cosmochemically allowed range (80–93 wt%), whereas C, O, and H were limited to: 0–4 wt%, 0–3 wt%, and 0–2.5 wt%, respectively. Finally, S was determined from the condition S=100–X, where X = (Fe+Ni+Co+C+O+H). Within this S range, we considered the subset covering 3 wt% to 11 wt%. The resultant core compositions were then converted to mean densities based on thermodynamic solution models constructed from experimental data (see appendix B) and shown in Fig. 6.

From the distributions, we can make the following observations: 1) density decreases almost linearly with increasing C content; 2) relative to C, density is much less affected by variations in the abundance of O; 3) for given C and O abundances, density decreases with increasing amounts of S, as expected; 4) density is most strongly influenced by the abundance of H; and most importantly, 5) a subset of the computed densities overlap with those determined from the joint geophysical-cosmochemical method (grey bars). In particular, we find that core compositions with S≈9 wt%, C⩾3 wt%, O⩽2.5 wt%, and H≈0.5 wt%, are compatible with the upper range of the geophysically-determined mean core density. This supports the notion of Mars as a volatile-rich planet (Wänke and Dreibus, 1994). The possible ranges (upper limits) in light elements in the core derived here are summarised in Table 3.

Comparison with the light element abundances derived in the previous section shows that although the geophysical constraints can be met, this appears only to be possible if O and H are present at, or even slightly in excess, of their respective upper limits. While this might suggest that the geophysical requirements of a less dense core are difficult to meet, it nevertheless shows, in view of the caveats and the modelling uncertainties, that a Mar-

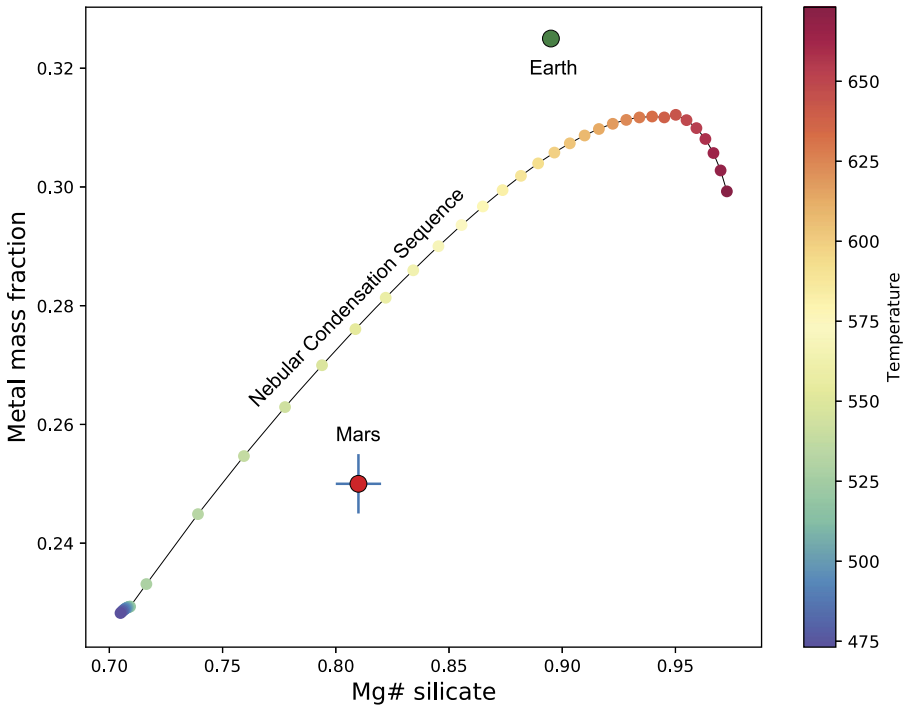

Fig. 7. The mass fraction of metallic components relative to silicates (Fe-Ni alloy + FeS)/(Fe-Ni alloy + FeS + silicate) as a function of Mg# in the silicate material condensing in equilibrium with a cooling nebular gas of composition given by Lodders (2003) at a nominal total pressure of 10^{-4} bar. The calculations were performed at 5 K intervals using FactSage 8.0 (Bale et al., 2009). The chemical evolution of the condensed solids defines a general trend of decreasing metal- and sulfide components with decreasing Mg#, reflecting the progressive oxidation of metallic iron (Fe^0) into ferrous iron (Fe^{2+}). The relative bulk properties of the Earth and Mars (green and red circles, respectively) are consistent with the latter containing more low-temperature material with a higher fraction of oxidised iron.

tian core composition with a density in the upper part of the range 6000–6300 kg/m^3 is not entirely impossible. To reduce the complement of light elements in the core requires increasing core density, which, in turn, implies lowering core radius. From a geophysical point of view, however, decreasing core radius below 1800 km is difficult on account of the relatively large value of the degree-2 Love number (see Table A.2), which measures the rigidity of the planet. This means that, even in the absence of the detection of the seismic core-reflection, the core size is relatively well-constrained on the basis of the geodetic data (e.g., Khan et al., 2018; Bagheri et al., 2019). This observation is supported by separate inversions of the geophysical data that showed that the mean core radius changed from 1836 km if only the InSight seismic data were considered to 1815 km in the case of geodetic data only, while the mean core density remained unchanged (Stähler et al., 2021).

If core density is indeed controlled by the concentrations of S, C, O, and H, then core formation conditions and/or volatile contents of early accreted material may have been considerably different from the aforementioned assumptions. On the basis of multi-stage core formation models, for example, Brennan et al. (2020) found that Ni and Co in the Martian mantle are best explained if the average equilibration pressure took place around ∼9-13 GPa, or about half of the present-day core-mantle-boundary pressure. If true, this would preclude larger amounts of both O and H, and would restrict their concentrations to levels at least an order of magnitude lower than the limits reported in Table 3.

7.2. Implications for the origin of Mars

Our results indicate that, in order to match the geophysically- and cosmochemically-estimated mean core density, Mars must have accumulated a substantial quantity of volatile elements. The high volatile contents required, in conjunction with elevated mantle FeO contents (and a low core/mantle ratio) relative to those of Earth, provide a qualitative link between Mars' present-day chemical make-up and its accretion environment. This is because, during cooling of the solar nebula, homogeneous equilibria in the gas phase consume CO(g) and H_2(g) to produce H_2O(g) and CH_4(g) at lower temperatures, thereby decreasing the H_2/H_2O of the gas and thus increasing the fO_2 of the system (Larimer and Bartholomay, 1979) with concomitant oxidation of Fe metal to FeO. Hence, as cooling proceeds, condensates are expected to become more volatile-rich and more oxidised.

To quantify the expected change progressive nebular cooling has on the chemistry of the condensed solids, and by extension accreting material, Gibbs Free Energy minimisation of the nebular gas composition given by Lodders (2003) is performed at 5 K increments (Fig. 7) using FactSage 8.0 (Bale et al., 2009). The results show that a decrease in the Mg# of the silicate material with cooling is observed as more O condenses, and reaches that observed in the Martian mantle (Mg#=0.81) at temperatures near ∼500 K, whereas that for Earth (Mg#=0.89) is achieved at higher temperatures, close to 650 K. Because the bulk iron content of the solids is constant, iron is distributed according to the equilibrium $Fe+\frac{1}{2}O_2$=FeO, which shifts to the right as temperature falls, leading to a commensurate decrease in metal mass fraction in the condensed solids. Although this simple analysis is instructive, planet forming processes are doubtless more complex than those depicted in Fig. 7, and involve not only the re-equilibration of metal- and silicate-attending energetic collisions (Rubie et al., 2015), but a stochastic collection of material from wide feeding zones that condensed to different extents (Wetherill, 1994). Nevertheless, this exercise serves to illustrate that, in relative terms compared to the Earth, a greater proportion of material rich in volatile elements, notably H and C, with an accordingly higher FeO/Fe ratio, is likely to have contributed to the formation of Mars. These conclusions are consistent with Mars' present-day semi-major axis, suggesting it accreted material at larger heliocentric distances than Earth.

Whether Mars acquired its FeO- and volatile-rich composition during the lifetime of the nebular gas prior to its dispersal, or owing to the accretion of a higher proportion of volatile-rich planetesimals from the outer solar system is not distinguishable from the chemical evidence presented above. Isotopic data, in particular Hf-W systematics (Dauphas and Pourmand, 2011; Kruijer et al., 2017; Bouvier et al., 2018), point to the rapid growth of Mars as a stranded embryo within a few million years after the formation of CAIs (Calcium-Aluminium-rich inclusions, taken as t_0). Over these timescales, the nebular gas is likely to still have been extant ($t_{dispersal} \sim 4$ Myr, Wang et al. (2017)), leading to the possibility that Mars accreted, if only partially, in the presence of an H_2-rich gas. In this context, Saito and Kuramoto (2018) envisaged a dense proto-atmosphere around Mars, consisting of a solar nebular gas component potentially reaching surface pressures of several kbars. Such a dense atmosphere may act as insulating blanket, keeping proto-Mars partially molten and the amounts of dissolved volatiles in the magma ocean sufficiently high, such that H may have reached or even exceeded the upper limit reported in Table 3.

Alternatively, N-body simulations of terrestrial planet accretion from planetesimals (Rubie et al., 2015) indicate that the outer terrestrial planets typically accrete higher proportions of volatile-rich material than their inner counterparts. The models of Rubie et al. (2015) in which Mars-analogue planets accrete in $\leq$ 10 Myr have bulk H_2O contents between 0 and 5000 ppm (compared to $\sim$ 1000 ppm for Earth), and FeO contents between 5–20 wt % (8 wt % for Earth). Although their results cannot be used to predict the composition of Mars, they qualitatively indicate it should be a more water-rich body than the Earth. Both mechanisms, therefore, may be viable ways of introducing H and other volatiles into the Martian mantle during its accretion.

The inherent degeneracy of assuming that the extant catalogue of chondrites and achondrites accreted to form Mars, together with the volatile nature of likely key light elements in the Martian core (C, H, and S) preclude any unique, cosmochemically-derived estimate of its core composition. We suggest that additional direct, spatially-resolved measurements of the physical properties of the Martian core, namely sound velocities and densities (e.g., Badro et al., 2014), will be key in better constraining its light element composition.

Our prediction that the mean FeO content of the Martian mantle lies close to 13.5 wt % is testable by performing melting experiments that succeed in producing magmatic liquids parental to the SNC meteorites. Importantly, such a lower FeO content compared to previous estimates (15–18 wt %, Wänke and Dreibus (1994); Yoshizaki and McDonough (2020)) implies decompression melting and hence magmatism would have been less widespread in the early history of Mars than previously thought. This arises due to the positive dependence of the solidus temperatures of peridotites and other ultramafic rocks, likely analogues for the Martian mantle, on their Mg# (Kogiso et al., 2004; Herzberg et al., 2000). In detail, this effect is relatively minor, with a dT/dMg# of $\sim$5 K (i.e., a 5 K increase in the solidus temperature for an increase in 0.01 Mg#), but likely becomes important integrated over the geological history of Mars. For the previous estimate of Mg# near 0.75, our data indicates a $\sim$ 30 K increase in solidus temperature of the mean Martian mantle with Mg# of 0.81. A similar dependence is observed on liquidus temperatures (Kogiso et al., 2004), such that more magnesian magma oceans should crystallise more rapidly than their lower Mg# counterparts, all else being equal.

8. Conclusion

With the acquisition of seismic data from Mars, we are finally able to directly probe the interior from the surface of the planet. On the basis of direct and surface- and core-reflected seismic phases, in combination with a set of global geophysical data and a cosmochemical approach that focuses on major elements and the extant correlation between Fe/Si and Fe/Mg that is observed in planetary materials, we have been able to obtain a novel composition of Mars. The new mantle composition contains markedly less FeO than the canonical models of Dreibus and Wänke and others. The core of Mars must contain a substantial complement of light elements to match a mean core density around 6150 kg/m^3. Based on geochemical arguments, the most plausible are, in order of abundance by weight, S ($\approx$9 %), C ($\geq$3%), O ($\leq$2.5%), and H ($\leq$0.5%). These elevated light element components relative to Earth's core indicate that Mars is a more volatile-rich planet than our own. The high FeO content of the Martian mantle, in conjunction with its high FeO/Fe ratio and volatile-rich core are consistent with its accretion of higher proportions of cooler material, likely reflecting its greater heliocentric distance relative to Earth. Continued analysis of the InSight seismic data in the extended mission period is expected to provide 5–10 additional good events to confirm the current observations and advance our understanding of the seismic structure of the core through observation of core-traversing waves. Of equal interest will be the search for a solid inner core that, if present, would represent an important anchoring point for understanding core composition, thermal state, and dynamics.

CRediT authorship contribution statement

A. Khan: Conceptualization, Data curation, Formal analysis, Investigation, Methodology, Software, Validation, Visualization, Writing – original draft, Writing – review & editing. **P.A. Sossi:** Conceptualization, Data curation, Formal analysis, Investigation, Methodology, Software, Validation, Visualization, Writing – original draft, Writing – review & editing. **C. Liebske:** Conceptualization, Data curation, Formal analysis, Investigation, Methodology, Software, Validation, Visualization, Writing – original draft, Writing – review & editing. **A. Rivoldini:** Methodology, Software, Writing – review & editing. **D. Giardini:** Writing – review & editing.

Declaration of competing interest

The authors declare that they have no known competing financial interests or personal relationships that could have appeared to influence the work reported in this paper.

Acknowledgements

We are grateful to Jeff Taylor and Youxue Zhang for thoughtful reviews. P.A.S. is grateful to the Swiss National Science Foundation (SNSF) for funding via Ambizione Grant 180025. The InSight seismic event catalogue (comprising all events, including phase picks, up to 30 September) and waveform data are available from the IRIS-DMC and SEIS-InSight data portal https://www.seis-insight.eu/en/science. The catalogue and waveform data have the identifiers http://doi.org/10.12686/a6 and https://doi.org/10.18715/SEIS.INSIGHT.XB_2016, respectively. All waveforms used in this paper are from the broad band sensor. All InSight seismic data used in this study are available from the IPGP data center: http://dx.doi.org/10.18715/SEIS.INSIGHT.XB_2016. We acknowledge NASA, CNES, partner agencies and Institutions (UKSA, SSO, DLR; JPL, IPGP-CNRS, ETHZ, IC, MPS-MPG) and the operators of JPL, SISMOC, MSDS, IRIS-DMC and PDS for providing SEED SEIS data. This is InSight contribution 228.

Appendix A. Seismic and global geophysical data

Table A.1
Summary of differential body wave phase picks. All travel times are relative to the main P-wave arrival of each event. Note that epicentral distances (Δ) indicate mean values. Uncertainties on Δ are around $\pm$1–2°. Events are labelled by mission Sol of occurrence and sub-labelled alphabetically for Sols with more than 1 event.

Event	Δ (°)	PP (s)	PPP (s)	S (s)	SS (s)	SSS (s)	ScS (s)
S0235b	29	17±5	36±5	167±5	195±5	–	511±3
S0407a	29	22±5	38±5	168±5	194±5	–	510±10
S0484b	29	22±5	40±5	172±5	–	–	513±20
S0173a	30	–	–	173±5	197±5	212±5	512±3
S0409d	30	–	–	177±5	–	–	510±5
S0189a	33	–	–	191±5	213±5	239±5	–
S0325a	40	29±8	–	230±5	257±5	280±5	500±20
S0185a	61	–	–	356±5	397±5	–	–
S0167b	72	55±8	–	418±5	466±5	502±5	–

Table A.2
Summary of Martian geophysical data, uncertainties, and sources. k_2 below refers to the main solar tidal period (12h19min). The values for the mean moment of inertia and mass have been updated by Rivoldini using the latest determination of G·M for Mars (Konopliv et al., 2020) with G = 6.67408(31)$\times 10^{-11}$ m^3/kg·s^2.

Observation	Symbol	Value (±uncertainty)	Source
Mean density	$\bar{\rho}$	3.9350±0.0012 g/cm^3	Rivoldini et al. (2011)
Mean moment of inertia	I/MR^2	0.3634±0.00006	Konopliv et al. (2020)
Love number	k_2	0.174±0.008	Konopliv et al. (2020)
Mean radius	R	3389.5 km	Seidelmann et al. (2002)
Mean mass	M	6.417·10^{23}±2.981·10^{19} kg	Konopliv et al. (2020)

Appendix B. Core EoS

To compute the depth-dependent properties of the core and its average density, we follow Rivoldini et al. (2011). We assume that the core is well mixed and that the temperature profile is adiabatic. The thermodynamic properties in the core are calculated from an equation of state that characterizes the physical properties of the Fe-O-S-C-H alloy.

In Rivoldini et al. (2011) the pressure p, gravity g, and temperature T inside the isotropic core are computed by solving Poisson's equation, the equation accounting for hydrostatic equilibrium, and the equation describing the adiabatic gradient in a convecting fluid. These ordinary differential equations are solved numerically subject to the following boundary conditions

$$g(0) = 0 \tag{B.1}$$

$$p(r_{cmb}) = p_{cmb} \tag{B.2}$$

$$T(r_{cmb}) = T_{cmb} \tag{B.3}$$

$$g(r_{cmb}) = \frac{G\, m_c}{r_{cmb}^2}, \tag{B.4}$$

where r_{cmb} is the core radius and G the gravitational constant. The pressure and temperature at the core mantle boundary p_{cmb} and T_{cmb} as well as the core mass m_c are prescribed. From these initial and boundary conditions, the pressure and temperature at the center of the planet and the core radius can be determined.

The equation of state of the liquid Fe-O-S-C-H core alloy is calculated under the premise that the five constituents mix ideally. We adopt this simplifying approach because of a lack of relevant thermodynamic properties required to describe the liquid solution over the large concentration range considered in this study. In our approach we use the following end-members: liquid Fe (Komabayashi, 2014), liquid FeS (Morard et al., 2018), liquid FeO (Komabayashi, 2014), liquid Fe_3C (Shimoyama et al., 2016; Morard et al., 2017), and solid FeH (Badding et al., 1992). We use the equation of state of solid FeH because of absence of an equation for the liquid state. To account for the density difference between solid and liquid FeH, we decrease the density of the liquid by 2%.

The thermodynamic properties required to solve the aforementioned ordinary differential equations are the density, the thermal expansivity, and the isobaric heat capacity. The density of the liquid Fe-O-S-C-H alloy is computed from its molar mass and volume V. At a given pressure and temperature, V can be written as

$$V = \chi_{\mathrm{Fe}} V_{\mathrm{Fe}} + \chi_{\mathrm{FeO}} V_{\mathrm{FeO}} + \chi_{\mathrm{FeS}} V_{\mathrm{FeS}} + \chi_{\mathrm{Fe_3C}} V_{\mathrm{Fe_3C}} + \chi_{\mathrm{FeH}} V_{\mathrm{FeH}}, \tag{B.5}$$

where the χ_i and the V_i are the molar fraction and molar volume of end-member i, respectively, and $\chi_{\mathrm{Fe}} + \chi_{\mathrm{FeO}} + \chi_{\mathrm{FeS}} + \chi_{\mathrm{Fe_3C}} + \chi_{\mathrm{FeH}} = 1$. The thermal expansivity is computed from Eq: (B.5) (Poirier, 2000, e.g.) by applying its thermodynamic definition. The molar mass and isobaric heat capacity of the alloy are computed similarly to the volume from the contribution of each end-member.

Appendix C. Inversion

Table C.1
Model parameters and prior ranges (prior information). Note that we only invert for primary parameters; secondary parameters are conditional on primary parameters. Primary parameters are all log-uniformly distributed.

Model Parameters	Prior Range	Description
V_S	2–4.2 km/s	Crustal S-wave velocity
α	1.65–1.85	Crustal $V_P/V_(S)$ scaling
β	0.8–1.15	Crustal ρ/V_S scaling
T′	473–1273 K	Crust-mantle interface temperature
Z′	20–100 km	Crustal thickness (primary)
Z_{lit}	100–600 km	Lithospheric thickness (primary)
T_{lit}	1273–1873 K	Temperature at Z_{lit} (primary)
X	variable	Mantle composition (primary)
R_{core}	1300–3000 km	Core radius (primary)
ρ_{core}	5–10 g/cm^3	Mean core density (primary)
h	0–100 km	Source depth (primary)
Δ	0°–180°	Epicentral distance (primary)
M	–	Equilibrium mineralogy (secondary)
V_P, V_S	–	Mantle P- and S-wave speed (secondary)
ρ	–	Mantle density (secondary)

To solve the inverse problem posited here, we make use of the probabilistic approach of Mosegaard and Tarantola (1995). In the Bayesian framework, the solution to the inverse problem $\mathbf{d} = \mathrm{g}(\mathbf{m})$, where $\mathbf{d}$ is the data vector consisting of the observations and g is an operator that maps a model parameter vector $\mathbf{m}$ into data $\mathbf{d}$, is given as

$$\sigma(\mathbf{m}) = k\eta(\mathbf{m})\mathcal{L}(\mathbf{m}), \tag{C.1}$$

where k is a normalization constant, $\eta(\mathbf{m})$ is the prior probability distribution on model parameters (summarised in Table C.1), $\mathcal{L}(\mathbf{m})$ is the likelihood function, which can be interpreted as a measure of misfit between the observations and the predictions from model $\mathbf{m}$, and $\sigma(\mathbf{m})$ is the posterior model parameter distribution that embodies the solution to the inverse problem. The particular form of $\mathcal{L}(\mathbf{m})$ is determined by the observations, the uncertainties, and the data noise model.

Following Khan et al. (2021) and Stähler et al. (2021), we assume that the errors can be modelled using an exponential probability density (L_1-norm), as a result of which the likelihood function takes the form

$$\mathcal{L}(\mathbf{m}) \propto \exp\left(-\sum_{\mathrm{j}} \frac{|\mathrm{d}^{\mathrm{j}}_{\mathrm{obs}} - \mathrm{d}^{\mathrm{j}}_{\mathrm{cal}}(\mathbf{m})|}{\sigma_{\mathrm{j}}} - \sum_{\alpha} \frac{|\mathrm{d}^{\alpha}_{\mathrm{obs}} - \mathrm{d}^{\alpha}_{\mathrm{cal}}(\mathbf{m})|}{\sigma_{\alpha}}\right) \tag{C.2}$$

where $\mathrm{d}_{\mathrm{cal}}(\mathbf{m})$ and $\mathrm{d}_{\mathrm{obs}}$ denote observed and calculated differential travel times, respectively, σ differential travel time uncertainty, and j runs over the number of differential travel time picks (34), while α is either k_2, $\bar{\rho}$, or I/MR^2. We rely on the L_1-norm because the posterior probability density function is less affected by outliers (Tarantola, 2005; Khan and Mosegaard, 2002).

Appendix D. Martian geotherms

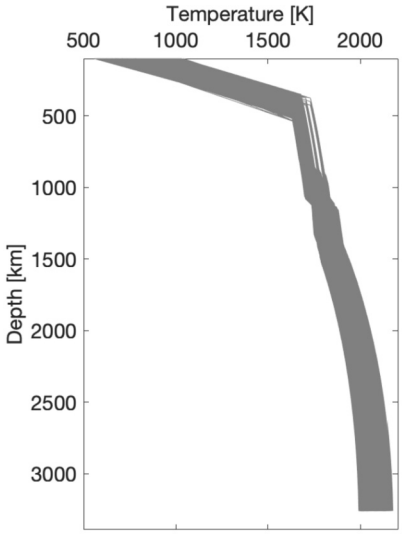

Fig. D.1. Geophysically-determined (inverted) present-day mantle areotherms for all the sampled compositions shown in Fig. 1. The areotherms overlap with those determined by Khan et al. (2021) and Stähler et al. (2021) (not shown), who find mantle potential temperatures in the range 1600–1700 K (cf. Table 1).

Appendix E. Hydrogen in the core

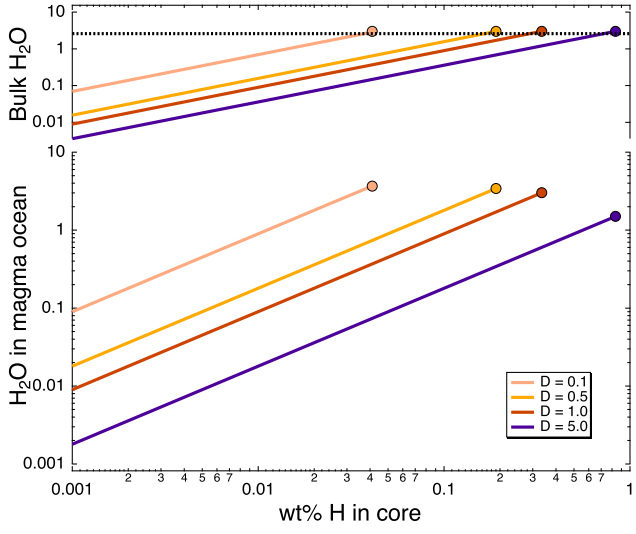

Fig. E.1. Relation between the concentration of hydrogen in the martian core and the required amount of this element dissolved in the magma ocean (lower panel) and its overall abundance for various partition coefficients (top panel) for various values of partition coefficient (D). Filled circles at the end of each of the lines indicate the maximum concentrations in either reservoir (mantle and core) for a total of 0.29 wt% H (black dashed line), assuming no atmospheric losses. Bulk hydrogen and the amount in the magma ocean are recalculated as H_2O equivalent.

References

Agee, C.B., Draper, D.S., 2004. Experimental constraints on the origin of martian meteorites and the composition of the martian mantle. Earth Planet. Sci. Lett. 224 (3), 415–429. https://doi.org/10.1016/j.epsl.2004.05.022.

Asahara, Y., Frost, D.J., Rubie, D.C., 2007. Partitioning of feo between magnesiowüstite and liquid iron at high pressures and temperatures: implications for the composition of the Earth's outer core. Earth Planet. Sci. Lett. 257 (3–4), 435–449. https://doi.org/10.1016/j.epsl.2007.03.006. Cited by 63.

Badding, J.V., Mao, H.K., Hemley, R.J., 1992. High-Pressure Crystal Structure and Equation of State of Iron Hydride: Implications for the Earth's Core. American Geophysical Union, pp. 363–371.

Badro, J., Côté, A.S., Brodholt, J.P., 2014. A seismologically consistent compositional model of Earth's core. Proc. Natl. Acad. Sci. 111 (21), 7542–7545.

Bagheri, A., Khan, A., Al-Attar, D., Crawford, O., Giardini, D., 2019. Tidal response of Mars constrained from laboratory-based viscoelastic dissipation models and geophysical data. J. Geophys. Res., Planets.

Bale, C.W., Bélisle, E., Chartrand, P., Decterov, S.A., Eriksson, G., Hack, K., Jung, I.-H., Kang, Y.-B., Melançon, J., Pelton, A.D., et al., 2009. Factsage thermochemical software and databases—recent developments. Calphad 33 (2), 295–311.

Banerdt, W.B., Smrekar, S.E., Banfield, D., Giardini, D., Golombek, M., Johnson, C.L., Lognonné, P., Spiga, A., Spohn, T., Perrin, C., Stähler, S.C., Antonangeli, D., Asmar, S., Beghein, C., Bowles, N., Bozdag, E., Chi, P., Christensen, U., Clinton, J., Collins, G.S., Daubar, I., Dehant, V., Drilleau, M., Fillingim, M., Folkner, W., Garcia, R.F., Garvin, J., Grant, J., Grott, M., Grygorczuk, J., Hudson, T., Irving, J.C.E., Kargl, G., Kawamura, T., Kedar, S., King, S., Knapmeyer-Endrun, B., Knapmeyer, M., Lemmon, M., Lorenz, R., Maki, J.N., Margerin, L., McLennan, S.M., Michaut, C., Mimoun, D., Mittelholz, A., Mocquet, A., Morgan, P., Mueller, N.T., Murdoch, N., Nagihara, S., Newman, C., Nimmo, F., Panning, M., Pike, W.T., Plesa, A.-C., Rodriguez, S., Rodriguez-Manfredi, J.A., Russell, C.T., Schmerr, N., Siegler, M., Stanley, S., Stutzmann, E., Teanby, N., Tromp, J., van Driel, M., Warner, N., Weber, R., Wieczorek, M., 2020. Initial results from the InSight mission on Mars. Nat. Geosci. (ISSN 1752-0894) 13 (3), 183–189. https://doi.org/10.1038/s41561-020-0544-y.

Bouvier, L.C., Costa, M.M., Connelly, J.N., Jensen, N.K., Wielandt, D., Storey, M., Nemchin, A.A., Whitehouse, M.J., Snape, J.F., Bellucci, J.J., et al., 2018. Evidence for extremely rapid magma ocean crystallization and crust formation on Mars. Nature 558 (7711), 586–589.

Boynton, W.V., Taylor, G.J., Evans, L.G., Reedy, R.C., Starr, R., Janes, D.M., Kerry, K.E., Drake, D.M., Kim, K.J., Williams, R.M.S., Crombie, M.K., Dohm, J.M., Baker, V., Metzger, A.E., Karunatillake, S., Keller, J.M., Newsom, H.E., Arnold, J.R., Brückner, J., Englert, P.A.J., Gasnault, O., Sprague, A.L., Mitrofanov, I., Squyres, S.W., Trombka, J.I., d'Uston, L., Wänke, H., Hamara, D.K., 2007. Concentration of H, Si, Cl, K, Fe, and Th in the low- and mid-latitude regions of Mars. J. Geophys. Res., Planets 112 (E12). https://doi.org/10.1029/2007JE002887.

Brennan, M.C., Fischer, R.A., Irving, J.C.E., 2020. Core formation and geophysical properties of Mars. Earth Planet. Sci. Lett. 530. https://doi.org/10.1016/j.epsl.2019.115923.

Clesi, V., Bouhifd, M.A., Bolfan-Casanova, N., Manthilake, G., Schiavi, F., Raepsaet, C., Bureau, H., Khodja, H., Andrault, D., 2018. Low hydrogen contents in the cores of terrestrial planets. Sci. Adv. 4 (3).

Clinton, J., Ceylan, S., van Driel, M., Giardini, D., Staehler, S.C., Böse, M., Charalambous, C., Dahmen, N.L., Horleston, A., Kawamura, T., Khan, A., Orhand-Mainsant, G., Scholz, J.-R., Euchner, F., Banerdt, W.B., Lognonne, P., Banfield, D., Beucler, E., Kedar, S., Panning, M., Perrin, C., Pike, W.T., Smrekar, S.E., Spiga, A., Stott, A.E., 2020. The marsquake catalogue from InSight, sols 0-478. Phys. Earth Planet. Inter. https://doi.org/10.31219/osf.io/ws967.

Collinet, M., Médard, E., Charlier, B., Vander Auwera, J., Grove, T.L., 2015. Melting of the primitive martian mantle at 0.5-2.2 GPa and the origin of basalts and alkaline rocks on Mars. Earth Planet. Sci. Lett. 427, 83–94. https://doi.org/10.1016/j.epsl.2015.06.056.

Connolly, J.A.D., 2009. The geodynamic equation of state: what and how. Geochem. Geophys. Geosyst. (ISSN 1525-2027) 10 (10), Q10014. https://doi.org/10.1029/2009GC002540.

Connolly, J.A.D., Khan, A., 2016. Uncertainty of mantle geophysical properties computed from phase equilibrium models. Geophys. Res. Lett. 43 (10), 5026–5034. https://doi.org/10.1002/2016GL068239.

Cottaar, S., Koelemeijer, P., 2021. The interior of Mars revealed. Science 373 (6553), 388–389. https://doi.org/10.1126/science.abj8914.

Dahmen, N.L., Clinton, J.F., Ceylan, S., van Driel, M., Giardini, D., Khan, A., Stähler, S.C., Böse, M., Charalambous, C., Horleston, A., Kawamura, T., Orhand-Mainsant, G., Scholz, J.-R., Euchner, F., Pike, W.T., Weber, R.C., Lognonné, P., Banerdt, W.B., 2021. Super high frequency events: a new class of events recorded by the InSight seismometers on Mars. J. Geophys. Res., Planets 126 (2). https://doi.org/10.1029/2020JE006599.

Dalou, C., Hirschmann, M.M., von der Handt, A., Mosenfelder, J., Armstrong, L.S., 2017. Nitrogen and carbon fractionation during core–mantle differentiation at shallow depth. Earth Planet. Sci. Lett. 458, 141–151. https://doi.org/10.1016/j.epsl.2016.10.026. Cited by 40.

Dasgupta, R., Chi, H., Shimizu, N., Buono, A.S., Walker, D., 2013. Carbon solution and partitioning between metallic and silicate melts in a shallow magma ocean: implications for the origin and distribution of terrestrial carbon. Geochim. Cosmochim. Acta 102, 191–212.

Dauphas, N., Pourmand, A., 2011. Hf–W–Th evidence for rapid growth of Mars and its status as a planetary embryo. Nature 473 (7348), 489–492.

Davies, C.J., Pommier, A., 2018. Iron snow in the martian core? Earth Planet. Sci. Lett. 481, 189–200. https://doi.org/10.1016/j.epsl.2017.10.026.

Davis, F.A., Humayun, M., Hirschmann, M.M., Cooper, R.S., 2013. Experimentally determined mineral/melt partitioning of first-row transition elements (frte) during partial melting of peridotite at 3 GPa. Geochim. Cosmochim. Acta 104, 232–260.

Elkins-Tanton, L.T., Parmentier, E.M., Hess, P.C., 2003. Magma ocean fractional crystallization and cumulate overturn in terrestrial planets: implications for Mars. Meteorit. Planet. Sci. 38 (12), 1753–1771. https://doi.org/10.1111/j.1945-5100.2003.tb00013.x.

Fichtner, C.E., Schmidt, M.W., Liebske, C., Bouvier, A.-S., Baumgartner, L.P., 2021. Carbon partitioning between metal and silicate melts during Earth accretion. Earth Planet. Sci. Lett. 554. https://doi.org/10.1016/j.epsl.2020.116659.

Fischer, R.A., Nakajima, Y., Campbell, A.J., Frost, D.J., Harries, D., Langenhorst, F., Miyajima, N., Pollok, K., Rubie, D.C., 2015. High pressure metal–silicate partitioning of ni, co, v, cr, si, and o. Geochim. Cosmochim. Acta 167, 177–194.

Garcia, R.F., Khan, A., Drilleau, M., Margerin, L., Kawamura, T., Sun, D., Wieczorek, M.A., Rivoldini, A., Nunn, C., Weber, R.C., Marusiak, A.G., Lognonné, P., Nakamura, Y., Zhu, P., 2019. Lunar seismology: an update on interior structure models. Space Sci. Rev. 215 (8). https://doi.org/10.1007/s11214-019-0613-y.

Giardini, D., Lognonné, P., Banerdt, W.B., Pike, W.T., Christensen, U., Ceylan, S., Clinton, J.F., van Driel, M., Stähler, S., Böse, M., Garcia, R.F., Khan, A., Panning, M., Perrin, C., Banfield, D., Beucler, E., Charalambous, C., Euchner, F., Horleston, A., Jacob, A., Kawamura, T., Kedar, S., Orhand-Mainsant, G., Scholz, J.-R., Smrekar, S., Spiga, A., Agard, C., Antonangeli, D., Barkaoui, S., Barrett, E., Combes, P., Conejero, V., Daubar, I., Drilleau, M., Ferrier, C., Gabsi, T., Gudkova, T., Hurst, K., Karakostas, F., King, S., Knapmeyer, M., Knapmeyer-Endrun, B., Llorca-Cejudo, R., Lucas, A., Luno, L., Margerin, L., McClean, J., Mimoun, D., Murdoch, N., Nimmo, F., Nonon, M., Pardo, C., Rivoldini, A., Rodriguez Manfredi, J.A., Samuel, H., Schimmel, M., Stott, A.E., Stutzman, E., Teanby, N., Warren, T., Weber, R., Wieczorek, M., Yana, C., 2020. The seismicity of Mars. Nat. Geosci. 13, 205–212. https://doi.org/10.1038/s41561-020-0539-8.

Herzberg, C., Raterron, P., Zhang, J., 2000. New experimental observations on the anhydrous solidus for peridotite klb-1. Geochem. Geophys. Geosyst. 1 (11).

Hin, R.C., Coath, C.D., Carter, P.J., Nimmo, F., Lai, Y.-J., von Strandmann, P.A.P., Willbold, M., Leinhardt, Z.M., Walter, M.J., Elliott, T., 2017. Magnesium isotope evidence that accretional vapour loss shapes planetary compositions. Nature 549 (7673), 511–515.

Hirschmann, M.M., 2016. Constraints on the early delivery and fractionation of Earth's major volatiles from C/H, C/N, and C/S ratios. Am. Mineral. 101 (3), 540–553. https://doi.org/10.2138/am-2016-5452.

Khan, A., Connolly, J.A.D., 2008. Constraining the composition and thermal state of Mars from inversion of geophysical data. J. Geophys. Res., Planets 113, E07003. https://doi.org/10.1029/2007JE002996.

Khan, A., Mosegaard, K., 2002. An inquiry into the lunar interior: a nonlinear inversion of the apollo lunar seismic data. J. Geophys. Res., Planets 107 (E6), 3-1–3-23. https://doi.org/10.1029/2001JE001658.

Khan, A., Pommier, A., Neumann, G.A., Mosegaard, K., 2013. The lunar moho and the internal structure of the moon: a geophysical perspective. Tectonophysics 609, 331–352. https://doi.org/10.1016/j.tecto.2013.02.024.

Khan, A., Liebske, C., Rozel, A., Rivoldini, A., Nimmo, F., Connolly, J.A.D., Plesa, A.-C., Giardini, D., 2018. A geophysical perspective on the bulk composition of Mars. J. Geophys. Res., Planets 123 (2), 575–611. https://doi.org/10.1002/2017JE005371.

Khan, A., Ceylan, S., van Driel, M., Giardini, D., Lognonné, P., Samuel, H., Schmerr, N.C., Stähler, S.C., Duran, A.C., Huang, Q., Kim, D., Broquet, A., Charalambous, C., Clinton, J.F., Davis, P.M., Drilleau, M., Karakostas, F., Lekic, V., McLennan, S.M., Maguire, R.R., Michaut, C., Panning, M.P., Pike, W.T., Pinot, B., Plasman, M., Scholz, J.-R., Widmer-Schnidrig, R., Spohn, T., Smrekar, S.E., Banerdt, W.B., 2021. Upper mantle structure of Mars from InSight seismic data. Science 373 (6553), 434–438. https://doi.org/10.1126/science.abf2966.

Knapmeyer-Endrun, B., Panning, M.P., Bissig, F., Joshi, R., Khan, A., Kim, D., Lekić, V., Tauzin, B., Tharimena, S., Plasman, M., Compaire, N., Garcia, R.F., Margerin, L., Schimmel, M., Stutzmann, É., Schmerr, N., Bozdağ, E., Plesa, A.-C., Wieczorek, M.A., Broquet, A., Antonangeli, D., McLennan, S.M., Samuel, H., Michaut, C., Pan, L., Smrekar, S.E., Johnson, C.L., Brinkman, N., Mittelholz, A., Rivoldini, A., Davis, P.M., Lognonné, P., Pinot, B., Scholz, J.-R., Stähler, S., Knapmeyer, M., van Driel, M., Giardini, D., Banerdt, W.B., 2021. Thickness and structure of the martian crust from InSight seismic data. Science 373 (6553), 438–443. https://doi.org/10.1126/science.abf8966.

Kogiso, T., Hirschmann, M.M., Pertermann, M., 2004. High-pressure partial melting of mafic lithologies in the mantle. J. Petrol. 45 (12), 2407–2422.

Komabayashi, T., 2014. Thermodynamics of melting relations in the system Fe-FeO at high pressure: implications for oxygen in the Earth's core. J. Geophys. Res., Solid Earth, 2014JB010980.

Konopliv, A.S., Park, R.S., Rivoldini, A., Baland, R.-M., Le Maistre, S., Van Hoolst, T., Yseboodt, M., Dehant, V., 2020. Detection of the Chandler wobble of Mars from orbiting spacecraft. Geophys. Res. Lett. 47 (21), e2020GL090568. https://doi.org/10.1029/2020GL090568.

Kruijer, T.S., Kleine, T., Borg, L.E., Brennecka, G.A., Irving, A.J., Bischoff, A., Agee, C.B., 2017. The early differentiation of Mars inferred from Hf–W chronometry. Earth Planet. Sci. Lett. 474, 345–354.

Larimer, J.W., Bartholomay, M., 1979. The role of carbon and oxygen in cosmic gases: some applications to the chemistry and mineralogy of enstatite chondrites. Geochim. Cosmochim. Acta 43 (9), 1455–1466.

Liebske, C., Khan, A., 2019. On the principal building blocks of Mars and Earth. Icarus 322, 121–134. https://doi.org/10.1016/j.icarus.2019.01.014.

Lodders, K., Fegley, B., 1997. An oxygen isotope model for the composition of Mars. Icarus 126, 373–394. https://doi.org/10.1006/icar.1996.5653.

Lodders, K., 2003. Solar system abundances and condensation temperatures of the elements. Astrophys. J. 591 (2), 1220.

Lognonné, P., Johnson, C., 2007. 10.03 - Planetary seismology. In: Schubert, G. (Ed.), Treatise on Geophysics. Elsevier, Amsterdam, pp. 69–122.

Lognonné, P., Banerdt, W.B., Giardini, D., Pike, W.T., Christensen, U., Laudet, P., de Raucourt, S., Zweifel, P., Calcutt, S., Bierwirth, M., Hurst, K.J., Ijpelaan, F., Umland, J.W., Llorca-Cejudo, R., Larson, S.A., Garcia, R.F., Kedar, S., Knapmeyer-Endrun, B., Mimoun, D., Mocquet, A., Panning, M.P., Weber, R.C., Sylvestre-Baron, A., Pont, G., Verdier, N., Kerjean, L., Facto, L.J., Gharakanian, V., Feldman, J.E., Hoffman, T.L., Klein, D.B., Klein, K., Onufer, N.P., Paredes-Garcia, J., Petkov, M.P., Willis, J.R., Smrekar, S.E., Drilleau, M., Gabsi, T., Nebut, T., Robert, O., Tillier, S., Moreau, C., Parise, M., Aveni, G., Charef, S.B., Bennour, Y., Camus, T., Dandonneau, P.A., Desfoux, C., Lecomte, B., Pot, O., Revuz, P., Mance, D., ten Pierick, J., Bowles, N.E., Charalambous, C., Delahunty, A.K., Hurley, J., Irshad, R., Liu, H., Mukherjee, A.G., Standley, I.M., Stott, A.E., Temple, J., Warren, T., Eberhardt, M., Kramer, A., Kühne, W., Miettinen, E.-P., Monecke, M., Aicardi, C., André, M., Baroukh, J., Borrien, A., Bouisset, A., Boutte, P., Brethomé, K., Brysbaert, C., Carlier, T., Deleuze, M., Desmarres, J.M.M., Dilhan, D., Doucet, C., Faye, D., Faye-Refalo, N., Gonzalez, R., Imbert, C., Larigauderie, C., Locatelli, E., Luno, L., Meyer, J.-R., Mialhe, F., Mouret, J.M.M., Nonon, M., Pahn, Y., Paillet, A., Pasquier, P., Perez, G., Perez, R., Perrin, L., Pouilloux, B., Rosak, A., de Larclause, I.S., Sicre, J., Sodki, M., Toulemont, N., Vella, B., Yana, C., Alibay, F., Avalos, O.M., Balzer, M.A., Bhandari, P., Blanco, E., Bone, B.D., Bousman, J.C., Bruneau, P., Calef, F.J., Calvet, R.J., D'Agostino, S.A., de los Santos, G., Deen, R.G., Denise, R.W., Ervin, J., Ferraro, N.W., Gengl, H.E., Grinblat, F., Hernandez, D., Hetzel, M., Johnson, M.E., Khachikyan, L., Lin, J.Y., Madzunkov, S.M., Marshall, S.L., Mikellides, I.G., Miller, E.A., Raff, W., Singer, J.E., Sunday, C.M., Villalvazo, J.F., Wallace, M.C., Banfield, D., Rodriguez-Manfredi, J.A., Russell, C.T., Trebi-Ollennu, A., Maki, J.N., Beucler, E., Böse, M., Bonjour, C., Berenguer, J.L., Ceylan, S., Clinton, J., Conejero, V., Daubar, I., Dehant, V., Delage, P., Euchner, F., Estève, I., Fayon, L., Ferraioli, L., Johnson, C.L.L., Gagnepain-Beyneix, J., Golombek, M., Khan, A., Kawamura, T., Kenda, B., Labrot, P., Murdoch, N., Pardo, C., Perrin, C., Pou, L., Sauron, A., Savoie, D., Stähler, S., Stutzmann, E., Teanby, N.A., Tromp, J., van Driel, M., Wieczorek, M., Widmer-Schnidrig, R., Wookey, J., 2019. SEIS: InSight's seismic experiment for internal structure of Mars. Space Sci. Rev. 215 (1), 12. https://doi.org/10.1007/s11214-018-0574-6.

Lognonné, P., Banerdt, W.B., Pike, W.T., Giardini, D., Christensen, U., Garcia, R.F., Kawamura, T., Kedar, S., Knapmeyer-Endrun, B., Margerin, L., Nimmo, F., Panning, M., Tauzin, B., Scholz, J.-R., Antonangeli, D., Barkaoui, S., Beucler, E., Bissig, F., Brinkman, N., Calvet, M., Ceylan, S., Charalambous, C., Davis, P., van Driel, M., Drilleau, M., Fayon, L., Joshi, R., Kenda, B., Khan, A., Knapmeyer, M., Lekic, V., McClean, J., Mimoun, D., Murdoch, N., Pan, L., Perrin, C., Pinot, B., Pou, L., Menina, S., Rodriguez, S., Schmelzbach, C., Schmerr, N., Sollberger, D., Spiga, A., Stähler, S., Stott, A., Stutzmann, E., Tharimena, S., Widmer-Schnidrig, R., Andersson, F., Ansan, V., Beghein, C., Böse, M., Bozdag, E., Clinton, J., Daubar, I., Delage, P., Fuji, N., Golombek, M., Grott, M., Horleston, A., Hurst, K., Irving, J., Jacob, A., Knollenberg, J., Krasner, S., Krause, C., Lorenz, R., Michaut, C., Myhill, B., Nissen-Meyer, T., ten Pierick, J., Plesa, A.-C., Quantin-Nataf, C., Robertsson, J., Rochas, L., Schimmel, M., Smrekar, S., Spohn, T., Teanby, N., Tromp, J., Vallade, J., Verdier, N., Vrettos, C., Weber, R., Banfield, D., Barrett, E., Bierwirth, E., Calcutt, S., Compaire, N., Johnson, C., Mance, D., Euchner, F., Kerjean, L., Mainsant, G., Mocquet, A., Rodriguez Manfredi, J.A., Pont, G., Laudet, P., Nebut, T., de Raucourt, S., Robert, O., Russell, C.T., Sylvestre-Baron, A., Tillier, S., Warren, T., Wieczorek, M., Yana, C., Zweifel, P., 2020. Constraints on the shallow elastic and anelastic structure of Mars from InSight seismic data. Nat. Geosci. 13, 213–220. https://doi.org/10.1038/s41561-020-0536-y.

Malavergne, V., Bureau, H., Raepsaet, C., Gaillard, F., Poncet, M., Surblé, S., Sifré, D., Shcheka, S., Fourdrin, C., Deldicque, D., Khodja, H., 2019. Experimental constraints on the fate of h and c during planetary core-mantle differentiation. Implications for the Earth. Icarus 321, 473–485. https://doi.org/10.1016/j.icarus.2018.11.027.

McSween Jr., H.Y., 1994. What we have learned about Mars from SNC meteorites. Meteoritics 29, 757–779.

McSween Jr., H.Y., McLennan, S.M., 2014. Mars. In: Turekian, K., Holland, H. (Eds.), Planets, Asteroids, Comets and the Solar System. Elsevier Science, pp. 251–300.

Mittelholz, A., Johnson, C.L., Feinberg, J.M., Langlais, B., Phillips, R.J., 2020. Timing of the martian dynamo: new constraints for a core field 4.5 and 3.7 ga ago. Sci. Adv. 6 (18). https://doi.org/10.1126/sciadv.aba0513.

Mohapatra, R.K., Murty, S.V.S., 2003. Precursors of Mars–constraints from nitrogen and oxygen isotopic compositions of martian meteorites. Meteorit. Planet. Sci. 38, 225–242. https://doi.org/10.1111/j.1945-5100.2003.tb00261.x.

Morard, G., Nakajima, Y., Andrault, D., Antonangeli, D., Auzende, A.L., Boulard, E., Cervera, S., Clark, A.N., Lord, O.T., Siebert, J., Svitlyk, V., Garbarino, G., Mezouar, M., 2017. Structure and density of Fe-C liquid alloys under high pressure. J. Geophys. Res., Solid Earth 122 (10), 7813–7823.

Morard, G., Bouchet, J., Rivoldini, A., Antonangeli, D., Roberge, M., Boulard, E., Denoeud, A., Mezouar, M., 2018. Liquid properties in the Fe-FeS system under moderate pressure: tool box to model small planetary cores. Am. Mineral.

Mosegaard, K., Tarantola, A., 1995. Monte Carlo sampling of solutions to inverse problems. J. Geophys. Res., Solid Earth (1978–2012) 100 (B7), 12431–12447.

Okuchi, T., 1997. Hydrogen partitioning into molten iron at high pressure: implications for Earth's core. Science 278 (5344), 1781–1784.

O'Neill, H.St.C., Palme, H., 1998. Composition of the silicate Earth: implications for accretion of and core formation. In: Jackson, I. (Ed.), The Earth's Mantle; Composition, Structure, and Evolution. Cambridge University Press, Cambridge, pp. 3–126.

O'Neill, H.St.C., Canil, D., Rubie, D.C., 1998. Oxide-metal equilibria to 2500°c and 25 GPa: implications for core formation and the light component in the Earth's core. J. Geophys. Res., Solid Earth 103 (6), 12239–12260. https://doi.org/10.1029/97jb02601. Cited by 98.

Palme, H., O'Neill, H.St.C., 2014. 3.1 - Cosmochemical estimates of mantle composition. In: Holland, H.D., Turekian, K.K. (Eds.), Treatise on Geochemistry - the Mantle and Core, second edition. Elsevier, Oxford, pp. 1–39.

Poirier, J.-P., 2000. Introduction to the Physics of the Earth's Interior. Cambridge University Press, Cambridge.

Ricolleau, A., Fei, Y., Corgne, A., Siebert, J., Badro, J., 2011. Oxygen and silicon contents of Earth's core from high pressure metal-silicate partitioning experiments. Earth Planet. Sci. Lett. 310 (3–4), 409–421. https://doi.org/10.1016/j.epsl.2011.08.004.

Rivoldini, A., Van Hoolst, T., Verhoeven, O., Mocquet, A., Dehant, V., 2011. Geodesy constraints on the interior structure and composition of Mars. Icarus 2, 451–472.

Rogers, A.D., Hamilton, V.E., 2015. Compositional provinces of Mars from statistical analyses of tes, grs, omega and crism data. J. Geophys. Res., Planets 120 (1), 62–91. https://doi.org/10.1002/2014JE004690.

Rubie, D.C., Jacobson, S.A., Morbidelli, A., O'Brien, D.P., Young, E.D., de Vries, J., Nimmo, F., Palme, H., Frost, D.J., 2015. Accretion and differentiation of the terrestrial planets with implications for the compositions of early-formed solar system bodies and accretion of water. Icarus 248, 89–108.

Rubie, D.C., Gessmann, C.K., Frost, D.J., 2004. Partitioning of oxygen during core formation on the Earth and Mars. Nature 429 (6987), 58–61. https://doi.org/10.1038/nature02473.

Rudge, J.F., Kleine, T., Bourdon, B., 2010. Broad bounds on earths accretion and core formation constrained by geochemical models. Nat. Geosci. 3 (6), 439–443. https://doi.org/10.1038/ngeo872.

Saito, H., Kuramoto, K., 2018. Formation of a hybrid-type proto-atmosphere on Mars accreting in the solar nebula. Mon. Not. R. Astron. Soc. 475 (1), 1274–1287. https://doi.org/10.1093/mnras/stx3176.

Samuel, H., Ballmer, M.D., Padovan, S., Tosi, N., Rivoldini, A., Plesa, A.-C., 2021. The thermo-chemical evolution of Mars with a strongly stratified mantle. J. Geophys. Res., Planets 126 (4). https://doi.org/10.1029/2020JE006613.

Seidelmann, P.K., Abalakin, V.K., Bursa, M., Davies, M.E., de Bergh, C., Lieske, J.H., Oberst, J., Simon, J.L., Standish, E.M., Stooke, P., Thomas, P.C., 2002. Report of the iau/iag working group on cartographic coordinates and rotational elements of the planets and satellites: 2000. Celest. Mech. Dyn. Astron. 82 (1), 83–111. https://doi.org/10.1023/A:1013939327465.

Shibazaki, Y., Ohtani, E., Terasaki, H., Suzuki, A., Funakoshi, K.-i., 2009. Hydrogen partitioning between iron and ringwoodite: implications for water transport into the martian core. Earth Planet. Sci. Lett. 287 (3–4), 463–470.

Shimoyama, Y., Terasaki, H., Urakawa, S., Takubo, Y., Kuwabara, S., Kishimoto, S., Watanuki, T., Machida, A., Katayama, Y., Kondo, T., 2016. Thermoelastic properties of liquid Fe-C revealed by sound velocity and density measurements at high pressure. J. Geophys. Res., Solid Earth 121 (11), 7984–7995.

Sossi, P.A., Nebel, O., Foden, J., 2016. Iron isotope systematics in planetary reservoirs. Earth Planet. Sci. Lett. 452, 295–308. https://doi.org/10.1016/j.epsl.2016.07.032.

Stähler, S.C., Khan, A., Banerdt, W.B., Lognonné, P., Giardini, D., Ceylan, S., Drilleau, M., Duran, A.C., Garcia, R.F., Huang, Q., Kim, D., Lekic, V., Samuel, H., Schimmel, M., Schmerr, N., Sollberger, D., Stutzmann, É., Xu, Z., Antonangeli, D., Charalambous, C., Davis, P.M., Irving, J.C.E., Kawamura, T., Knapmeyer, M., Maguire, R., Marusiak, A.G., Panning, M.P., Perrin, C., Plesa, A.-C., Rivoldini, A., Schmelzbach, C., Zenhäusern, G., Beucler, É., Clinton, J., Dahmen, N., van Driel, M., Gudkova, T., Horleston, A., Thomas Pike, W., Plasman, M., Smrekar, S.E., 2021. Seismic detection of the martian core. Science 373 (6553), 443–448. https://doi.org/10.1126/science.abi7730.

Steenstra, E.S., van Westrenen, W., 2018. A synthesis of geochemical constraints on the inventory of light elements in the core of Mars. Icarus 315, 69–78. https://doi.org/10.1016/j.icarus.2018.06.023.

Stevenson, D.J., 2001. Mars' core and magnetism. Nature 412, 214–219.

Stixrude, L., Lithgow-Bertelloni, C., 2011. Thermodynamics of mantle minerals - II. Phase equilibria. Geophys. J. Int. 184, 1180–1213. https://doi.org/10.1111/j.1365-246X.2010.04890.x.

Stixrude, L., Lithgow-Bertelloni, C., 2005. Mineralogy and elasticity of the oceanic upper mantle: origin of the low-velocity zone. J. Geophys. Res., Solid Earth 110 (B3). https://doi.org/10.1029/2004JB002965.

Tarantola, A., 2005. Inverse Problem Theory and Methods for Model Parameter Estimation, Volume XII. ISBN 978-0-89871-572-9.

Taylor, G.J., 2013. The bulk composition of Mars. Chem. Erde 73, 401–420. https://doi.org/10.1016/j.chemer.2013.09.006.

Taylor, G.J., Stopar, J.D., Boynton, W.V., Karunatillake, S., Keller, J.M., Brückner, J., Wänke, H., Dreibus, G., Kerry, K.E., Reedy, R.C., Evans, L.G., Starr, R.D., Martel, L.M.V., Squyres, S.W., Gasnault, O., Maurice, S., d'Uston, C., Englert, P., Dohm, J.M., Baker, V.R., Hamara, D., Janes, D.M., Sprague, A.L., Kim, K.J., Drake, D.M., McLennan, S.M., Hahn, B.C., 2007. Variations in K/Th on Mars. J. Geophys. Res. E, Planets 112 (3). https://doi.org/10.1029/2006JE002676.

Tsuno, K., Grewal, D.S., Dasgupta, R., 2018. Core-mantle fractionation of carbon in Earth and Mars: the effects of sulfur. Geochim. Cosmochim. Acta 238, 477–495.

Vacher, L.G., Piani, L., Rigaudier, T., Thomassin, D., Florin, G., Piralla, M., Marrocchi, Y., 2020. Hydrogen in chondrites: influence of parent body alteration and atmospheric contamination on primordial components. Geochim. Cosmochim. Acta 281, 53–66. https://doi.org/10.1016/j.gca.2020.05.007.

van Driel, M., Ceylan, S., Clinton, J.F., Giardini, D., Horleston, A., Margerin, L., Stähler, S.C., Böse, M., Charalambous, C., Kawamura, T., Khan, A., Orhand-Mainsant, G., Scholz, J.-R., Euchner, F., Knapmeyer, M., Schmerr, N., Pike, W.T., Lognonné, P., Banerdt, W.B., 2021. High-frequency seismic events on Mars observed by InSight. J. Geophys. Res., Planets 126 (2).

Wang, H., Weiss, B.P., Bai, X.-N., Downey, B.G., Wang, J., Wang, J., Suavet, C., Fu, R.R., Zucolotto, M.E., 2017. Lifetime of the solar nebula constrained by meteorite paleomagnetism. Science 355 (6325), 623–627.

Wang, Z., Becker, H., 2017. Chalcophile elements in martian meteorites indicate low sulfur content in the martian interior and a volatile element-depleted late veneer. Earth Planet. Sci. Lett. 463, 56–68.

Wänke, H., Dreibus, G., 1994. Chemistry and accretion history of Mars. Philos. Trans. R. Soc. Lond. Ser. A 349, 285–293. https://doi.org/10.1098/rsta.1994.0132.

Wasson, J.T., Kallemeyn, G.W., 1988. Compositions of chondrites. Philos. Trans. R. Soc. Lond. Ser. A, Math. Phys. Sci. 325 (1587), 535–544.

Wetherill, G.W., 1994. Provenance of the terrestrial planets. Geochim. Cosmochim. Acta 58 (20), 4513–4520.

Wood, B.J., Smythe, D.J., Harrison, T., 2019. The condensation temperatures of the elements: a reappraisal. Am. Mineral. 104 (6), 844–856.

Yoshizaki, T., McDonough, W.F., 2020. The composition of Mars. Geochim. Cosmochim. Acta 273, 137–162. https://doi.org/10.1016/j.gca.2020.01.011.

Yoshizaki, T., McDonough, W.F., 2021. Earth and Mars – distinct inner solar system products. Geochemistry, 125746. https://doi.org/10.1016/j.chemer.2021.125746.

Zharkov, V.N., Gudkova, T.V., 2005. Construction of martian interior model. Sol. Syst. Res. 39, 343–373. https://doi.org/10.1007/s11208-005-0049-7.